

Quantum transport of Dirac fermions in selected graphene nanosystems away from the charge-neutrality point

Adam Rycerz*

Institute for Theoretical Physics, Jagiellonian University, Łojasiewicza 11, PL–30348 Kraków, Poland

(Dated: December 17, 2024)

Peculiar electronic properties of graphene, including the universal dc conductivity and the pseudodiffusive shot noise, are usually attributed to a small vicinity of the charge-neutrality point, away from which electron's effective mass raises, and nanostructures in graphene start to behave similarly to familiar Sharvin contacts in semiconducting heterostructures hosting two-dimensional electron gas. Using the effective Dirac equation for low-energy excitations it can be shown that, as long as abrupt potential steps separate the sample area from the leads, some graphene-specific features can be identified even relatively far from the charge-neutrality point. Namely, the conductance is reduced, by a factor varying from $\pi/4$ to $(4 - \pi)$ (depending on the sample geometry) comparing to the standard Sharvin value, whereas the shot noise is amplified, with the Fano factor varying from $F \approx 0.1065$ to 0.125 . In this paper, we confront the results of earlier analytic considerations with numerical simulations of quantum transport on the honeycomb lattice, for selected systems containing up to 336,000 lattice sites, with different geometries for which considerations starting from the Dirac equation cannot be directly adapted. The results show that for a wedge-shape constriction with zigzag edges and approximately square shape of the narrowest section, the transport characteristics can be tuned from graphene-specific *sub-Sharvin* values to standard Sharvin values, depending on whether the electrostatic potential profile in the narrowest section is rectangular (i.e., has abrupt steps) or smooth (approximately parabolic). Similarly, the half-Corbino disk with zigzag edges and rectangular potential profile exhibits both the conductance and the noise close to the sub-Sharvin values. In contrast, for a circular quantum dot with two narrow openings and irregular edges, the conductance is close to the Sharvin value, and the Fano factor approaches the value of $F \approx 0.25$, characterizing the symmetric chaotic cavity. For a similar quantum dot with a hole, eliminating direct trajectories connecting the two openings, the conductance is reduced by a factor close to $\pi/4$, coinciding with the sub-Sharvin value, but the Fano factor is almost unaffected remaining close to $F \approx 0.25$. This suggests that, in experimental attempt to verify the predictions for sub-Sharvin transport regime, one should focus rather on nanosystems with relatively wide sample openings, for which the scatterings on edges are insignificant next to the scatterings on sample-lead interfaces.

I. INTRODUCTION

There are few phenomena in nature for which the results of measurements of physical quantities are given directly by the fundamental constants of nature, leaving even the question of the actual number of fundamental constants open [1, 2]. In the second half of the last century, two phenomena from this group were discovered and theoretically described: the quantum Hall effect [3–6] and the Josephson effect [7], which are currently used as the basis for the standards of units of resistance and electric voltage in the SI system, i.e., the ohm [8] and the volt [9]. The discovery of the two-dimensional allotrope of carbon, graphene, made at the beginning of the 21st century [10, 11] allowed for the improvement of the Ohm standard based on the quantum Hall effect [8]. (Some peculiar features of the Josephson effect in graphene were also pointed out [12, 13].) Moreover, it turned out that several material characteristics of graphene, such as the conductivity [14, 15] or visible light absorption [16, 17], are given by the fundamental constants or dimensionless numerical coefficients. The sub-Poissonian shot noise (quantified by the Fano factor $F = 1/3$) [18–21] and the anomalous Lorentz number [22–25] for charge-neutral graphene also can be regarded as examples of such characteristics. Although measurements

of these quantities with metrological accuracy are not possible yet, the scientific community have undoubtedly gained unique opportunities to test a theoretical model, which is the effective two-dimensional Dirac-Weyl equation for monolayer graphene [26, 27].

The author and Witkowski have recently find, using the effective Dirac equation, that for doped graphene samples of highly-symmetric shapes (namely, the rectangle with smooth edges and the Corbino disk) the conductance is reduced, whereas the shot noise is amplified, comparing to standard Sharvin values [28, 29]. The reduction (or amplification) is maximal when abrupt potential steps separate the sample area from the leads; for instance, the conductance $G \approx (\pi/4) G_{\text{Sharvin}}$ (with $G_{\text{Sharvin}} = g_0 k_F W / \pi$ [30–32], g_0 the conductance quantum, k_F the Fermi wavenumber, and W the sample width [33]) for the rectangle or the narrow disk (i.e., the inner-to-outer radii ratio $R_i/R_o \approx 1$), $G \approx (4 - \pi) G_{\text{Sharvin}}$ for the wide-disk limit ($R_i/R_o \ll 1$); the Fano factor $F \approx 1/8$ for the rectangle or the disk with $R_i/R_o \approx 1$, $F \approx 0.1065$ for the disk with $R_i/R_o \ll 1$. When the potential profile gets smoothen the above-listed *sub-Sharvin* values evolve towards $G \approx G_{\text{Sharvin}}$ and the Fano factor approaches the ballistic value of $F \approx 0$. Later, the discussion in analytical terms was extended on the nonzero magnetic field case [34, 35], showing that in a doped disk with $R_i/R_o \approx 1$ the vanishing conductance $G \rightarrow 0$ (notice that in the disk geometry the edge states are absent and the current is blocked at sufficiently high field except from narrow resonances via

*Corresponding author; e-mail: rycerz@th.if.uj.edu.pl.

Landau levels [36–40]) is accompanied by a non-trivial value of $F \approx 0.55$.

It is the purpose of this paper to extend the discussion of sub-Sharvin transport regime in graphene by going beyond the effective Dirac equation. In particular, we address the question how realistic (irregular) edges of a nanosystem carved out of the honeycomb lattice affect transport characteristics? For this purpose, we perform computer simulations of quantum transport for selected systems depicted schematically in Fig. 1 modeled within the tight-binding Hamiltonian. The results show that sub-Sharvin characteristics are closely reconstructed for relatively short and wide systems; for longer and more complex system with multiple constrictions some less obvious scenarios (including the sub-Sharvin conductance accompanied by the shot-noise power resembling a chaotic cavity) can be observed.

The remaining parts of the paper are organized as follows. In Sec. II, we present the Landauer-Büttiker formalism for a generic nanoscopic system and key literature results following from the effective Dirac equation for graphene at the charge-neutrality point as well as in the sub-Sharvin regime. Higher charge-transfer cumulants for graphene at and away from the charge-neutrality point are also discussed in Sec. II. Statistical distributions of transmission probabilities for different quantum-transport regimes, including the sub-Sharvin transport regime in graphene, are described in Sec. III. The tight-binding model of graphene and our main results concerning the conductance and the Fano factor for selected nanosystems (see Fig. 1) are presented in Sec. IV. The conclusions are given in Sec. V.

II. LANDAUER-BÜTTIKER TRANSPORT IN NANOSCOPIC SYSTEMS AND GRAPHENE

A. Remark on the origin of zero-temperature Landauer-Sharvin resistance

First, let's look for a concise answer to the question: *Where does electrical resistance come from at absolute zero?*

In the familiar Drude model of electrical conduction [41] electrons are assumed to constantly bounce between heavier, stationary lattice ions, allowing one to express the material specific resistivity as a function of the electron's effective mass, velocity, and the mean free path. In quantum-mechanical description of solids, Drude model provides a reasonable approximation as long as the Fermi wavelength remains much shorter than electron's mean free path and the conductor size.

The picture sketched above changes substantially when electric charge flows through a nanoscopic system, such as quantum point contact in semiconducting heterostructure [31], a carbon nanotube [42], or monoatomic quantum wire [43] (see Fig. 2, top part). Assuming for simplicity that such a system has no internal degrees of freedom leading to the degeneracy of quantum states, in other words — that in a sufficiently small energy range ΔE we have at most one quantum state (level) — we note that the time of flight of an electron

through the system is limited from below by the time-energy uncertainty relation

$$\Delta t \geq \frac{\hbar}{\Delta E}. \quad (1)$$

Next, by linking the energy range ΔE with the electrochemical potential difference in macroscopic electrodes (reservoirs) connected to the nanoscopic system (see Fig. 2, bottom part), we can write

$$\Delta E = \mu_L - \mu_R = eU, \quad (2)$$

where U denotes the difference in electrostatic potential on both sides of the system, and is the elementary charge (without sign). Combining the above equations we obtain the limit for the electric current flowing through the system,

$$I = \frac{e}{\Delta t} \leq \frac{e^2}{\hbar} U, \quad (3)$$

which means that the electrical conductivity

$$G = \frac{I}{U} \leq \frac{e^2}{\hbar}. \quad (4)$$

We thus see that the uncertainty principle of energy and time leads to a finite value of the conductivity, and therefore to a nonzero value of the electrical resistance, of a nanoscopic system. By rigorous derivation, the upper bound in Eq. (4) is replaced by e^2/h , introducing the Landauer-Sharvin resistance in noninteracting electron systems [30, 44, 45]. Obviously, many-body effects may alter this conclusion substantially. For instance, the resistivity of graphene sample may drop below the Landauer-Sharvin bound due to hydrodynamic effects [46]. In twisted bilayer graphene, both the interaction-driven insulating and superconducting (i.e., resistance-free) phases were observed [47–49]. These issues are, however, beyond the scope of the present work.

B. The Landauer-Büttiker formula

At a temperature close to absolute zero ($T \rightarrow 0$) and in the limit of linear response, i.e., the situation in which the electrochemical potential difference also tends to zero ($\mu_L - \mu_R = eU \rightarrow 0$), it can be shown that the electrical conductivity of a nanoscopic system is proportional to the sum of transition probabilities for the so-called normal modes in the leads [50],

$$G = g_0 \sum_n T_n(E_F), \quad (5)$$

where g_0 denotes the conductance quantum; namely, $g_0 = 2e^2/h$ for systems exhibiting spin degeneracy (for graphene, we have $g_0 = 4e^2/h$ due to the additional degeneracy — called valley degeneracy — related to the presence of two nonequivalent Dirac points in the dispersion relation). The probabilities (T_n) are calculated by solving (exactly or approximately) the corresponding wave equation (Schrödinger or Dirac) for a fixed energy, which, given the assumptions

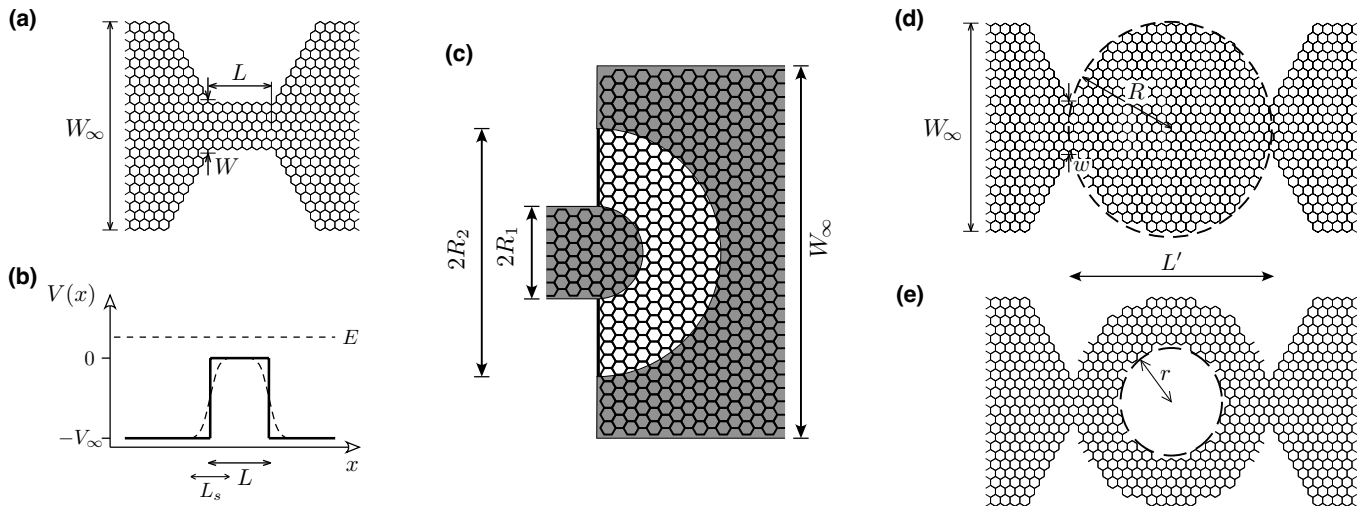


Figure 1: (a)–(e) Systems studied numerically in the work (schematic). (a) Constriction with zigzag edges containing a narrow rectangular section of the width W and the length L . (b) Corresponding potential profile. (c) Half Corbino disk (white area) with the inner radii R_1 and the outer radii R_2 attached to doped graphene leads with armchair edges (shaded areas). (d) Circular quantum dot of the radii R . The electrostatic potential profile (not shown) is same as in (b), but the steps are placed in the two narrowest sections of w width at a distance L' . (e) Circular quantum dot with a circular hole, of the radii r , in the center and the remaining parameters same as in (d).

made, can be identified with the Fermi energy E_F . Importantly, we perform the calculations under the additional assumption that there are so-called waveguides between the macroscopic reservoirs and the nanoscopic system, for which we can provide (for a fixed value of E_F) solutions in the form of propagating waves, the number of which is N_L or N_R , for the left or right waveguide, respectively (see Fig. 2). We also assume that a wave that reaches the waveguide-reservoir interface is never reflected. It is worth noting that the sum appearing in formula (5) is the trace of the transmission matrix, the value of which does not depend on the choice of the basis; therefore, it can be expected that the result does not depend on how precisely we construct the aforementioned waveguides, which, it is worth emphasising, are an auxiliary construction that usually has no direct physical interpretation. (For the same reason, the result will be the same whether we consider scattering from left to right or in the opposite direction.)

As mentioned above, the details of the calculations (or computer simulations) leading to the determination of the probability values (T_n) will depend on the geometry of the system under consideration. If waveguides are modelled as strips of fixed width (W), at the edges of which the wave function disappears, the normal modes have the form of plane waves [51], for which the longitudinal component of the wave vector (k_x) is continuous and the normal component (k_y) is quantized according to the rule

$$k_y^{(n)} = \frac{\pi n}{W}, \quad n = 1, 2, \dots \quad (6)$$

The calculations are particularly simple in cases where the central region (marked with a dark square in Fig. 2) differs from the leads only in that it contains an electrostatic potential that depends on the x coordinate (oriented along the main axis of the system), for example in the form of a rectangular barrier. Then the transmission matrix has a diagonal form

(no scattering between normal modes occurs), and in special cases, such as the rectangular barrier mentioned above, but also e.g. the parabolic potential considered by Kemble in 1935 [52], it is possible to provide compact analytical formulas.

We will not present the exact results here, but only point out that for solutions obtained by the mode-matching method for the Schrödinger equation, one can write approximately

$$T_n = T(k_y^{(n)}) \approx \begin{cases} 1 & \text{if } k_y \leq k_F, \\ 0 & \text{if } k_y > k_F, \end{cases} \quad (7)$$

which we write more briefly as $T_n \approx \Theta(k_F - k_y^{(n)})$, with $\Theta(x)$ denoting the Heaviside step function. In Eq. (7) we introduce the wave vector k_F corresponding to the Fermi energy E_F (assuming for simplicity that the dispersion relation is isotropic) calculated with respect to the top of the potential barrier in the central region. Furthermore, assuming that there are many modes for which $k_y^{(n)} < k_F$ (which occurs if $k_F W \gg 1$), and therefore the summation in Eq. (5) can be replaced to a good approximation by integration, we obtain — via Eqs. (6) and (7) — the result known in the literature as the Sharvin conductance [30]

$$G_{\text{Sharvin}} \approx g_0 \frac{k_F W}{\pi}. \quad (8)$$

It is worth noting that the reasoning leading to Eq. (8) can be relatively easily applied to the case where the electrostatic potential in the central region is approximately constant and the width of the conducting region is a function of the position along the longitudinal axis (x), changing slowly enough that the scattering between normal modes can be neglected. The above-mentioned case is the so-called quantum point contact (QPC), shown schematically in Fig. 2 (top part), which can be realized in semiconductor heterostructures hosting a two-dimensional electron gas (2DEG) [50].

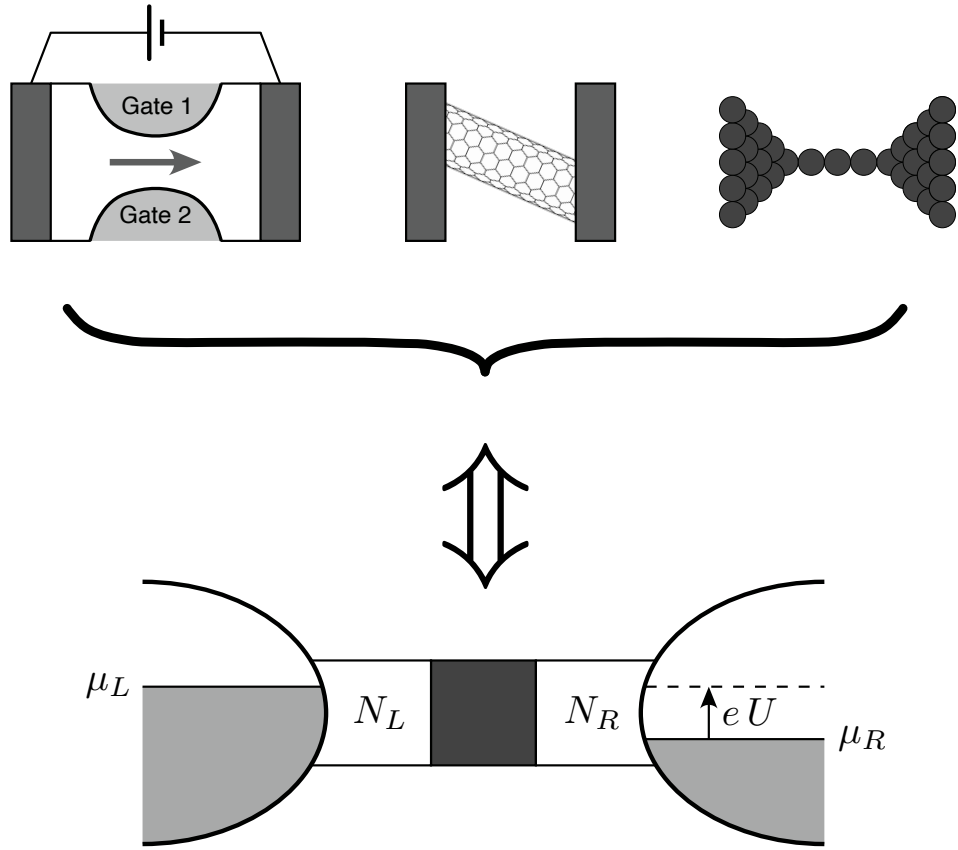


Figure 2: Physical suppositions behind the Landauer-Büttiker formalism. Top: Basic nanoscopic systems; from left: a quantum point contact (QPC) in semiconducting heterostructure, a carbon nanotube, and monoatomic quantum wire (each system is contacted by two electrodes and connected to a voltage source driving a current, as shown for QPC). Bottom: A theoretical model, containing the two macroscopic reservoirs (left and right) with fixed chemical potentials (μ_L , μ_R), waveguides with their numbers of normal modes (N_L , N_R), and the central region (dark square) for which transmission probabilities (T_n) need to be determined by solving a relevant quantum-mechanical wave equation.

C. Shot noise and counting statistics

The second quantity, besides electrical conductivity, that characterizes nanoscopic systems at temperatures close to absolute zero is the shot-noise power. For the sake of brevity, let us point out the basic facts: First, the electric charge Q flowing through the system shown schematically in Fig. 2 (lower part) in a short time interval Δt is a random variable. Second, the expectation value of such a variable is closely related to the electrical conductivity G in the linear-response limit,

$$\langle Q \rangle = GU\Delta t \quad (U \rightarrow 0). \quad (9)$$

The reason the measured value of Q fluctuates at successive time intervals is due to the discrete (granular) nature of the electric charge.

Assuming (for the moment) that electrons jump from one reservoir to another completely independently, we conclude that the charge flow is a Poisson process, or more precisely, that the quantity Q/e follows the Poisson distribution; the variance is therefore proportional to the expectation value given by Eq. (9),

$$\langle Q^2 - \langle Q \rangle^2 \rangle_{\text{Poisson}} = e\langle Q \rangle = eU\Delta t g_0 \sum_n T_n. \quad (10)$$

More generally, m -th central moment can be written as

$$\langle \langle Q^m \rangle \rangle_{\text{Poisson}} \equiv \langle (Q - \langle Q \rangle)^m \rangle_{\text{Poisson}} = e^{m-1} \langle Q \rangle, \quad (11)$$

with the integer $m \geq 1$.

The Fano factor, quantifying the shot-noise power, is defined as the ratio of the actual measured variance of the charge flowing through the system to the variance given by Eq. (10), or more precisely

$$F = \frac{\langle Q^2 - \langle Q \rangle^2 \rangle}{\langle Q^2 - \langle Q \rangle^2 \rangle_{\text{Poisson}}} = 1 - \frac{\sum_n T_n^2}{\sum_n T_n}. \quad (12)$$

(For compact derivation, see e.g. Ref. [50].) In the following, we have limited our considerations to long time intervals such that $eU\Delta t \gg \hbar$; hence F characterizes the zero-frequency noise, not to be confused with the celebrated $1/f$ noise in electronic systems [53]. A generalization of Eq. (12) for finite times (and nonzero temperatures) is also possible [54].

In particular, it follows from Eq. (12) that the Poisson limit ($F \rightarrow 1$) is realized in the case of a tunnel junction, for which we have $T_n \ll 1$ for each n . This is a completely different case than the ballistic system considered above, which exhibits Sharvin conductance; then, replacing the summation

with integration as before and using the approximation given by Eq. (7), we obtain

$$F_{\text{Sharvin}} \approx 1 - \frac{\int dk_y (\Theta(k_F - k_y))^2}{\int dk_y \Theta(k_F - k_y)} \approx 0. \quad (13)$$

In general, for fermionic systems we always have $0 < F < 1$; the factor $1 - T_n$ appearing in the numerator in Eq. (12) is a consequence of the Pauli exclusion principle. In the case of the idealized ballistic system we have $F = 0$, see Eq. (13), which means that the electron count (Q/e) does not fluctuate with time. One could say that the electrons avoid each other so much that they "march" at equal intervals. (Of course, this is only possible at absolute zero temperature, otherwise additional thermal noise appears, i.e. the Nyquist-Johnson noise proportional to the conductivity value, whose influence we have ignored here; see Ref. [50].)

In an attempt to determine higher charge cumulants, it is convenient to introduce characteristic function

$$\Lambda(\chi) = \langle \exp(i\chi Q/e) \rangle, \quad (14)$$

such that

$$\langle \langle Q^m \rangle \rangle \equiv \langle (Q - \langle Q \rangle)^m \rangle = e^m \left. \frac{\partial^m \ln \Lambda(\chi)}{\partial (i\chi)^m} \right|_{\chi=0}. \quad (15)$$

Assuming $U > 0$ for simplicity, we arrive at the Levitov-Lesovik formula [50, 54]

$$\ln \Lambda(\chi) = \frac{g_0 U \Delta t}{e} \sum_n \ln [1 + T_n (e^{i\chi} - 1)], \quad (16)$$

expressing the full counting for noninteracting fermions.

Substitution of the above into Eq. (15) with $m = 1$ and $m = 2$ reproduces (respectively) Eqs. (5) and (12). Analogously, for $m = 3$ and $m = 4$, we get

$$R_3 \equiv \frac{\langle \langle Q^3 \rangle \rangle}{\langle \langle Q^3 \rangle \rangle_{\text{Poisson}}} = \left(\sum_n T_n - 3 \sum_n T_n^2 + 2 \sum_n T_n^3 \right) / \sum_n T_n, \quad (17)$$

$$R_4 \equiv \frac{\langle \langle Q^4 \rangle \rangle}{\langle \langle Q^4 \rangle \rangle_{\text{Poisson}}} = \left(\sum_n T_n - 7 \sum_n T_n^2 + 12 \sum_n T_n^3 - 6 \sum_n T_n^4 \right) / \sum_n T_n. \quad (18)$$

For the Sharvin regime, see Eq. (7),

$$(R_3)_{\text{Sharvin}} \approx (R_4)_{\text{Sharvin}} \approx 0. \quad (19)$$

D. Scattering of Dirac fermions in two dimensions

Using the introductory information gathered above, we will now calculate — with some additional simplifying assumptions — the electrical conductivity as well as the higher charge cumulants of a graphene strip. The effective wave equation for itinerant electrons in this two-dimensional crystal is the Dirac-Weyl equation, the detailed derivation of which can be found, e.g., in Katsnelson's textbook [15], and which can be written in the form

$$[v_F \mathbf{p} \cdot \boldsymbol{\sigma} + V(x)] \Psi = E \Psi, \quad (20)$$

where the energy-independent Fermi velocity is given by $v_F = \sqrt{3}t_0 a / (2\hbar)$, where $t_0 \approx 2.7$ eV denotes the nearest-neighbor hopping integral in the graphene plane and $a = 0.246$ nm is the lattice constant (as a result, the approximate value of v_F is about 10^6 m/s, which is several times lower than typical Fermi velocities in metals). The remaining symbols in Eq. (20) are the quantum mechanical momentum op-

erator $\mathbf{p} = -i\hbar(\partial_x, \partial_y)$ (the notation ∂_j here means differentiation with respect to the selected coordinate, $j = x, y$), $\boldsymbol{\sigma} = (\sigma_x, \sigma_y)$ is a vector composed of Pauli matrices [55], and the electrostatic potential energy $V(x)$ is assumed to depend only on the position along the principal axis of the system.

The above assumptions imply that we can look for solutions to Eq. (20) in the form of a two-component (i.e., spinor) wave function

$$\Psi = \begin{pmatrix} \phi_a \\ \phi_b \end{pmatrix} e^{ik_y y}, \quad (21)$$

where ϕ_a and ϕ_b are functions of x . By substituting the above ansatz into Eq. (20) we obtain a system of ordinary differential equations

$$\phi'_a = k_y \phi_a + i \frac{E - V(x)}{\hbar v_F} \phi_b, \quad (22)$$

$$\phi'_b = i \frac{E - V(x)}{\hbar v_F} \phi_a - k_y \phi_b, \quad (23)$$

where the primes on the left-hand side denote derivatives with respect to x . We see that in the system of Eqs. (22), (23) the quantities k_y and E play the role of parameters on which the solutions depend (in the following, when calculating, among others, the electrical conductivity, we will identify the electron's energy with the Fermi energy by setting $E = E_F$).

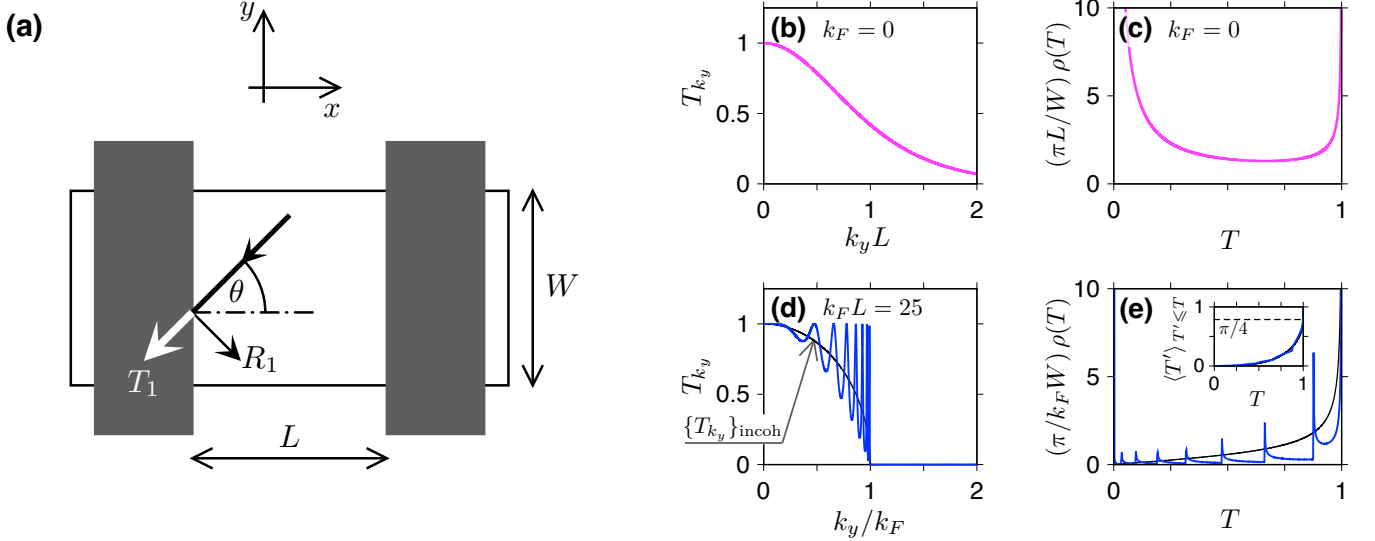


Figure 3: (a) Rectangular graphene sample (white area) of the width W contacted to the leads (dark areas) at a distance L . The coordinate system (x, y) is also shown. Scattering of Dirac electrons at a sample-lead interface for the incident angle θ is characterized by the transmission (T_1) and the reflection (R_1) coefficients given by Eq. (29). (b) Transmission probability for a double barrier [see Eq. (30)] as a function of the transverse momentum k_y and (c) the corresponding distribution of transmission probabilities at the Dirac point $k_F = 0$ (with $k_F = |E|/\hbar v_F$). (d,e) Same as (b,c) but the doping fixed at $k_F L = 25$. Blue lines represent the exact results, black lines depict the approximation $\{T_{k_y}\}_{\text{incoh}}$ given by Eq. (41). Inset in (e) shows the integrated distribution $\langle T' \rangle_{T' \leq T} = (\pi/k_F W) \int_0^T dT' T' \rho(T')$ for both the exact $\rho(T)$ [blue line] and the approximation given by Eq. (61) [black line]. The sub-Sharvin value of $\langle T \rangle = \pi/4$ is depicted with dashed horizontal line.

At this point it is worth to comment on the problem of quantizing the value of the transverse momentum (k_y) in Eqs. (22), (23). Assuming that the component of the current density perpendicular to the axis of the graphene strip disappears at its edges (i.e., for $y = 0$ and $y = W$, see Fig. 3(a)), what is known as the so-called mass confinement [56], we get a slightly different quantization than in the case of the Schrödinger system, see Eq. (6), namely

$$k_y^{(n)} = \frac{\pi(n + 1/2)}{W}, \quad n = 0, 1, 2, \dots \quad (24)$$

In practice, however, the assumptions made in the following part mean that when calculating measurable quantities (G , F , etc.) we will approximate the sums appearing in Eqs. (5), (12), (17), (18), with integrals with respect to dk_y ; the quantization change described above is therefore insignificant for further considerations.

The solution of the system of Eqs. (22), (23) is particularly simple in the case if the electrostatic potential energy, i.e. the function $V(x)$, is piecewise constant. Then, the solutions in individual sections (i.e., areas where $V(x)$ is constant) have the form of plane waves. For instance, for $E > V(x)$ waves traveling in the positive (+) and negative (-) directions along the x axis, look as follows

$$\phi^{(+)} = \begin{pmatrix} 1 \\ e^{i\theta} \end{pmatrix} e^{ik_x x}, \quad \phi^{(-)} = \begin{pmatrix} 1 \\ -e^{-i\theta} \end{pmatrix} e^{-ik_x x}, \quad (25)$$

where we have defined

$$\begin{aligned} e^{i\theta} &= (k_x + ik_y)/k_F, \\ k_F &= (E - V(x))/\hbar v_F, \\ \text{and } k_x &= \sqrt{k_F^2 - k_y^2}. \end{aligned} \quad (26)$$

For $E < V(x)$, propagating-wave solutions also exist (this is, by the way, the main difference between the solutions of the massless Dirac equation and the Schrödinger equation, which leads in particular to the phenomenon known as Klein tunneling [57, 58]) and differ from those given in Eq. 25 only in some signs. We leave the straightforward derivation to the reader.

At the interface of regions differing in the (locally constant) value of $V(x)$, we perform a matching of wave functions, which for the two-dimensional Dirac equation reduces to solving the continuity conditions for both spinor components [59]. For instance, if we consider the scattering from the right side of the discontinuity to the left side, we write

$$t\phi^{(L,-)} = \phi^{(R,-)} + r\phi^{(R,+)}, \quad (27)$$

where the spinor functions with indices L and R differ in the values of k_F and k_x [see Eqs. (25), (26)], but are characterized by the same value of k_y . Since the considerations concern the interface between the graphene sample and the graphene region covered with a metal electrode (see Fig. 3(a)), the calculations can be simplified by adopting the model of a heavily doped electrode, in which we set $V(x) = -V_\infty$, where $V_\infty \rightarrow \infty$; we can then write the wave functions on the left in

asymptotic form

$$\phi^{(L,\pm)} \simeq \begin{pmatrix} 1 \\ \pm 1 \end{pmatrix}, \quad (28)$$

where we have omitted the phase factor, which is not important for further considerations. After substituting the above into Eq. (27), the calculations are straightforward; we now present the results for the transition and reflection probabilities

$$T_1 = |t|^2 = \frac{2 \cos \theta}{1 + \cos \theta}, \quad R_1 = |r|^2 = \frac{1 - \cos \theta}{1 + \cos \theta}, \quad (29)$$

which turn out to depend only on the angle of incidence θ of the plane wave, or — more precisely — on the value of $\cos \theta = \sqrt{1 - (k_y/k_F)^2}$. In particular, we see that for $\theta = 0$ we have $T_1 = 1$ (and $R_1 = 0$), which is a manifestation of the Klein tunneling mentioned above (let us emphasize that the potential barrier considered here has an infinite height).

The probability of passing through the entire graphene sample, i.e., through two electrostatic potential steps occurring at the sample-lead interface (see Fig. 3(a)), is most easily calculated using the double-barrier formula, the clear derivation of which can be found, e.g., in the Datta's handbook [60]

$$T_{12} = \frac{T_1 T_2}{1 + R_1 R_2 - 2\sqrt{R_1 R_2} \cos \phi}, \quad (30)$$

where a phase shift

$$\phi = k_x L = L\sqrt{k_F^2 - k_y^2}, \quad (31)$$

related to the propagation of a plane wave along the main axis x , is introduced. (Note here that the phase shift introduced in this manner also implies the assumption that any reflections from the side edges of the system do not change the value of k_y ; in practice, this implies that we restrict our considerations to systems for which $W \gg L$.) Assuming barrier symmetry, $T_2 = T_1$, $R_2 = R_1$, and substituting the formulas given in Eq. (29), we can now write T_{12} explicitly as a function of k_y and E ,

$$T_{12} = T_{k_y}(E) = \left[1 + \left(\frac{k_y}{\varkappa} \right)^2 \sin^2(\varkappa L) \right]^{-1}, \quad (32)$$

where

$$\varkappa = \begin{cases} \sqrt{k_F^2 - k_y^2}, & \text{for } |k_y| \leq k_F, \\ i\sqrt{k_y^2 - k_F^2}, & \text{for } |k_y| > k_F, \end{cases} \quad (33)$$

and the Fermi wave vector, assuming $V(x) = 0$ for the sample region, is equal to $k_F = |E|/(\hbar v_F)$. The absolute value in the last expression arises from the fact that formulas in Eq. (29) and the following results are identical for $E < 0$; we leave the verification of this property to the reader.

E. The conductivity, shot noise, and higher cumulants for ballistic graphene strip

The physical consequences of the above expression for the transition probabilities $T_{k_y}(E)$, see Eqs. (32) and (33), are now discussed for two physical situations: a charge-neutral sample ($k_F = 0$) and the Sharvin limit ($k_F W \gg 1$). (Unless otherwise stated, we also assume geometry with long, parallel sample-lead interfaces and $W \gg L$.)

In the first case ($k_F = 0$) we obtain $\varkappa = i|k_y|$ and can use the identity $\sin(ix) = i \sinh x$, resulting in a surprisingly simple expression

$$T_{k_y}(0) = \frac{1}{\cosh^2(k_y L)}, \quad (34)$$

visualized in Fig. 3(b). In the wide-sample limit, $W \gg L$, the sums appearing in the formulas for Landauer conductance G [see Eq. (5)], Fano factor F [Eq. (12)], and higher cumulants R_3 , R_4 [Eqs. (17) and (18)] can be approximated with integrals [see also Eq. (24)], leading to

$$\sum_n T_n(0) \approx \frac{W}{\pi} \int_0^\infty dk_y T_{k_y}(0) = \frac{W}{\pi L}, \quad (35)$$

$$\sum_n [T_n(0)]^2 \approx \frac{W}{\pi} \int_0^\infty dk_y (T_{k_y}(0))^2 = \frac{2}{3} \frac{W}{\pi L}, \quad (36)$$

or, more generally,

$$\sum_n [T_n(0)]^m \approx \frac{W}{2\sqrt{\pi} L} \frac{\Gamma(m)}{\Gamma(m + 1/2)} \quad \text{for } m > 0, \quad (37)$$

where $\Gamma(x)$ is the Euler gamma function. To facilitate future comparisons with other transport regimes, we will additionally define

$$\langle T^m \rangle_{k_F=0} = L \int_0^\infty dk_y (T_{k_y}(0))^m = \frac{\sqrt{\pi} \Gamma(m)}{2\Gamma(m + \frac{1}{2})}, \quad (38)$$

such that $\langle T \rangle_{k_F=0} = 1$. Taking into account the graphene-specific fourfold degeneracy of states due to the presence of spin and valley degrees of freedom (the conductance quantum is therefore $g_0 = 4e^2/h$), we obtain

$$G \approx \frac{4e^2}{\pi h} \frac{W}{L}, \quad F \approx 1 - \frac{2}{3} = \frac{1}{3}, \quad (39)$$

$$R_3 \approx \frac{1}{15}, \quad R_4 \approx -\frac{5}{512}. \quad (40)$$

The value of $G \propto W/L$ (instead of $G \propto W$, as in a typical ballistic system) means that charge-neutral graphene exhibits universal specific conductivity, $\sigma_0 = 4e^2/(\pi h)$, the value of which is additionally determined only by the universal constants of nature. The value of the Fano factor $F = 1/3$ is also not accidental, as it is a value characteristic for ohmic (disordered) conductors. (The same applies to higher cumulants.) In the context of graphene, the term *pseudodiffusive conductivity* is often used to emphasize that this ballistic system perfectly

emulates an ohmic conductor within the appropriate parameter range. It should be emphasized that the first two theoretical values, given in Eq. (39) and originally derived in Refs. [14] (conductance) and [18] (Fano factor), have been experimentally confirmed with satisfactory accuracy in 2008 [19]. (For the comprehensive theoretical discussion of full counting statistics for graphene at the Dirac point, see Ref. [61].)

In the Sharvin limit ($k_F W \gg 1$) the situation looks a bit different. We can then assume that the contribution of modes for which $k_y > k_F$ (i.e., *evanescent* modes) is negligible and limit the considerations to $k_y \leq k_F$. Next, we notice that as the values of $T_{k_y}(E)$ (or their powers) are summed, the $\sin^2(L\sqrt{k_F^2 - k_y^2})$ term of Eq. (32) oscillates rapidly, especially as k_y approaches k_F . Therefore, it seems reasonable to replace the sine argument with a random phase and average the result, which leads to the following approximation

$$T_{k_y}(E) \approx \{T_{k_y}\}_{\text{incoh}} = \frac{1}{\pi} \int_0^\pi \frac{d\varphi}{1 + (k_y^2/\varkappa^2) \sin^2 \varphi} = \sqrt{1 - (k_y/k_F)^2}, \quad (41)$$

where we used the table integral [62]

$$I(a, b) = \frac{1}{2\pi} \int_{-\pi}^\pi \frac{du}{a + b \cos u} = \frac{1}{\sqrt{a^2 - b^2}}, \quad \text{for } a > |b|, \quad (42)$$

substituting

$$u = 2\varphi, \quad a = \frac{1 - \frac{1}{2}\eta^2}{1 - \eta^2}, \quad b = a - 1 = \frac{\frac{1}{2}\eta^2}{1 - \eta^2}, \quad (43)$$

with $\eta = k_y/k_F$.

The comparison between the approximation given in Eq. (41) and the actual $T_{k_y}(E)$, see Eqs. (32), (33), for $k_F L = 25$, is presented in Fig. 3(d).

Eq. (41) is essentially the Dirac version of Eq. (7) describing a standard ballistic system; when calculating the Landauer

conductance, we can again approximate the summation by integration and obtain

$$G \approx \frac{g_0 W}{\pi} \int_0^{k_F} dk_y \{T_{k_y}\}_{\text{incoh}} = \frac{\pi}{4} G_{\text{Sharvin}}, \quad (44)$$

where we recall the value of Sharvin conductance given in Eq. (8). The prefactor $\pi/4$ is a consequence of the fact that in the last expression in Eq. (41), where previously there was a step function $\Theta(k_F - k_y)$, a term describing an arc of a circle has appeared; the conductance of graphene beyond the charge-neutrality point is therefore reduced compared to a typical ballistic system.

Interestingly, in deriving Eq. (44) we did not explicitly assume, as in Eq. (39), that the width to length ratio of the sample is $W/L \gg 1$; hypothetically, the result given in Eq. (44) can therefore be applied whenever the condition $k_F W \gg 1$ is satisfied, regardless of the value of W/L . In practice, however, it is difficult to imagine that the double-barrier transmission formula, Eq. (30), which is the basis of the entire reasoning, could be applied to samples that do not satisfy the $W/L \gg 1$ condition. It seems that in the case of graphene samples with $L \gtrsim W$, hard-to-control edge effects can significantly alter the conductivity [63]. We will address this issue later in this paper, but first let us calculate the approximate values of the Fano factor and higher cumulants in the Sharvin limit.

In order to construct the approximation analogous to this in Eq. (41), but for $T_{k_y}^2$, it is sufficient to calculate

$$\{T_{k_y}^2\}_{\text{incoh}} = \frac{1}{\pi} \int_0^\pi \frac{d\varphi}{[1 + (k_y^2/\varkappa^2) \sin^2 \varphi]^2} = \sqrt{1 - \eta^2} \left[1 - \frac{1}{2}\eta^2\right], \quad (45)$$

where we used the first derivative of $I(a, b)$, see Eqs. (42) and (43), with respect to a . More generally, the m -th power of T_{k_y} can be approximated by

$$\begin{aligned} \{T_{k_y}^m\}_{\text{incoh}} &= \frac{1}{\pi} \int_0^\pi \frac{d\varphi}{[1 + (k_y^2/\varkappa^2) \sin^2 \varphi]^m} = \frac{(-1)^{m-1}}{(m-1)!} \frac{\partial^{m-1}}{\partial a^{m-1}} I(a, b) \\ &= \frac{2^{m-1} \Gamma(m - \frac{1}{2}) a^{m-1}}{\sqrt{\pi} \Gamma(m) (a^2 - b^2)^{m-1/2}} {}_2F_1 \left(1 - \frac{m}{2}, \frac{1-m}{2}; \frac{3}{2} - m; 1 - \frac{b^2}{a^2}\right), \\ &= \frac{2^{m-1} \Gamma(m - \frac{1}{2})}{\sqrt{\pi} \Gamma(m)} \sqrt{1 - \eta^2} z^{-m+1} {}_2F_1 \left(1 - \frac{m}{2}, \frac{1-m}{2}; \frac{3}{2} - m; z\right), \quad \text{with } z = \frac{1 - \eta^2}{(1 - \frac{1}{2}\eta^2)^2}, \end{aligned} \quad (46)$$

where ${}_2F_1(\alpha, \beta; \gamma; z)$ is the hypergeometric function [64]. (Notice that for a positive integer m , $\alpha = 1 - \frac{m}{2}$ or $\beta = \frac{1-m}{2}$ is a non-positive integer, so the function reduces to a polynomial of z ; after multiplying by z^{-m+1} , the resulting expres-

sion can be further simplified to a degree $2m - 2$ polynomial of the variable η .) For $m = 1$ and $m = 2$, the above reproduces the results of Eqs. (41) and (45), respectively. The next

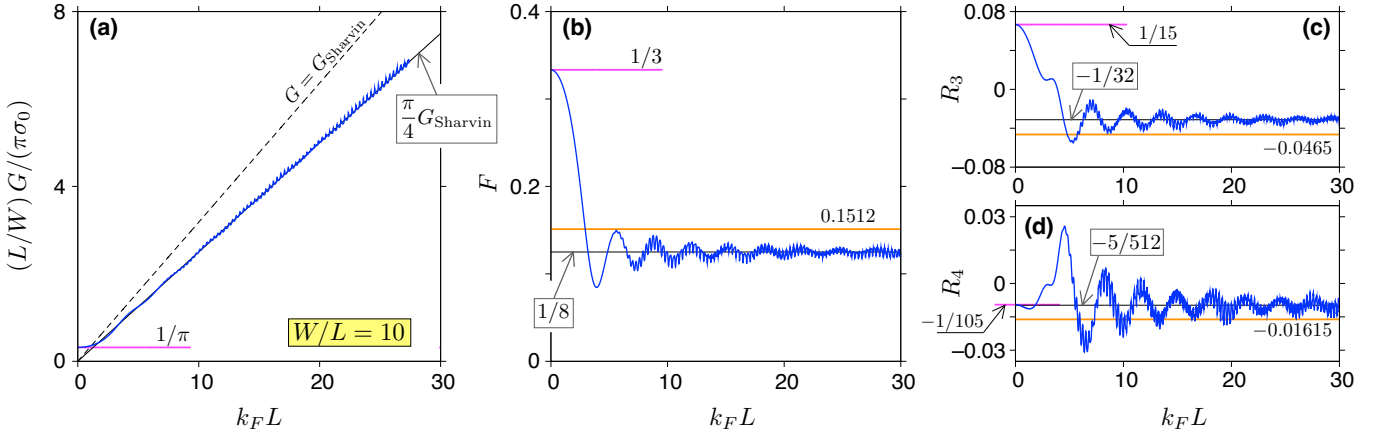


Figure 4: Conductance (a), Fano factor (b), third (c), and fourth (d) charge-transfer cumulant for graphene strip displayed as functions of the Fermi momentum (solid blue lines). The aspect ratio is fixed at $W/L = 10$. Dashed black line in (a) depicts the Sharvin conductance $G_{\text{Sharvin}} = g_0 k_F W / \pi$, with $g_0 = 4e^2/h$; the sub-Sharvin values, given by Eqs. (44), (51) are depicted with solid black lines in all panels. Short purple line (a–d) marks the pseudodiffusive value, see Eqs. (39), (40), approached for $k_F \rightarrow 0$. Wide orange lines (b–d) depict the values following from the approximated distribution of transmission probabilities $\rho_{\text{approx}}(T)$, see Eq. (61).

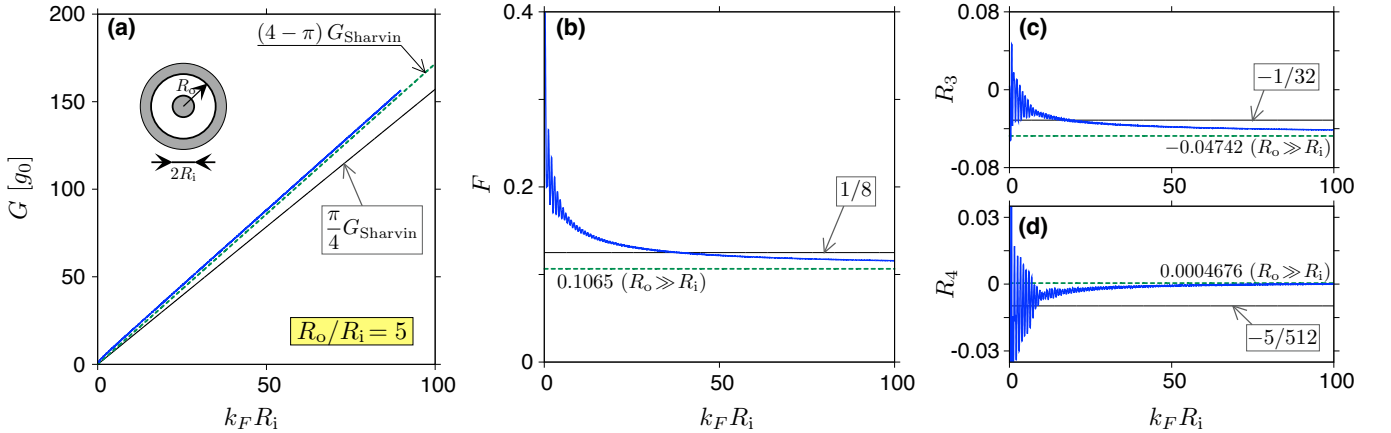


Figure 5: (a–d) Same as Fig. 4 but for the Corbino disk, see inset in (a), with the outer-to-inner radii ratio $R_o/R_i = 5$. Solid blue lines mark the exact results following from Eqs. (56), (57). Remaining lines mark the sub-Sharvin values relevant for the thin-disk limit $R_i/R_o \rightarrow 1$ [solid black] and for the narrow-opening limit, $R_i/R_o \rightarrow 0$, see Eq. (55) [dashed green].

two expressions are

$$\{T_{k_y}^3\}_{\text{incoh}} = \sqrt{1 - \eta^2} \left(1 - \eta^2 + \frac{3}{8}\eta^4 \right), \quad (47)$$

$$\{T_{k_y}^4\}_{\text{incoh}} = \sqrt{1 - \eta^2} \left(1 - \frac{\eta^2}{2} \right) \left(1 - \eta^2 + \frac{5}{8}\eta^4 \right). \quad (48)$$

Setting $[T_{k_y}(E)]^m \approx \{T_{k_y}^m\}_{\text{incoh}}$ for $m = 1, \dots, 4$, and approximating the summations occurring in Eqs. (12), (17), and (18) by integrations, namely,

$$\sum_n [T_n(E)]^m \approx \frac{k_F W}{\pi} \langle \{T_{k_y}^m\}_{\text{incoh}} \rangle \quad (49)$$

$$\text{with } \langle \{T_{k_y}^m\}_{\text{incoh}} \rangle = \int_0^1 d\eta \{T_{k_y}^m\}_{\text{incoh}}, \quad (50)$$

we obtain

$$F \approx \frac{1}{8}, \quad R_3 \approx -\frac{1}{23}, \quad R_4 \approx -\frac{5}{512}. \quad (51)$$

(For the first four numerical values of $\langle \{T_{k_y}^m\}_{\text{incoh}} \rangle$, see Table I.)

The surprising (non-zero) value of the shot noise in Eq. (51) is close to the experimental results obtained by Danneau *et al.* [19], which are in the range of $F = 0.10 \div 0.15$. (The aspect ratio of the sample used in this experiment was $W/L = 24$.) It should be emphasized that measuring the shot noise of nanoscopic devices containing components of different materials is rather challenging; there are also results in the literature that suggest that the dependence of the shot noise on the system filling is weak, with the value always close to the pseudodiffusive $F = 1/3$ [65]. Measurements of higher charge cumulants are so far missing.

In Fig. 4, the approximations for G , F , R_3 , and R_4 , both for $k_F = 0$ and for $k_F W \gg 1$, are compared with the actual values following from Eqs. (32), (33) for $T_{k_y}(E)$. Briefly speaking, the higher cumulant is considered, the larger value of $k_F W$ is necessary to observe the convergence to the sub-Sharvin limit; however, for $W/L = 10$ and for the heavily-doped leads, $k_F W \gtrsim 5$ is sufficient. The discussion of more realistic situations (finite doping in the leads, other sample shapes) is presented later in this paper.

F. The narrow-opening limit

Using the conformal mapping technique [20, 66], it can be shown that for charge-neutral graphene ($k_F = 0$), the pseudodiffusive values given in Eqs. (37), (39), (40) are essentially valid for an arbitrary sample shape, provided that the prefactor W/L (if present) is replaced by an appropriate geometry-dependent factor defined by the conformal transformation. In particular, when mapping the rectangle onto the Corbino disk, one needs to substitute $W/L \rightarrow 2\pi/\log(R_o/R_i)$, where R_o and R_i are the outer and inner disk radii (respectively), see Fig. 5(a). An additional condition is that the system must be in the multimode regime, i.e. $\log(R_o/R_i) \ll 1$ (or $R_i \approx R_o$) in the disk case. Otherwise, if $R_i \ll R_o$, a nonstandard tunneling behavior is observed, with $G \propto R_i/R_o$ and $F \rightarrow 1$ [20]. (Since the transport is governed by a single mode, we also have $R_3 \rightarrow 1$ and $R_4 \rightarrow 1$ in such a case.)

However, in the Sharvin limit ($k_F R_i \gg 1$ in the disk case), a different set of universal charge-transport characteristics is predicted [29]. Regardless of the exact size or shape of the outer sample-lead interface, one can assume that the double-barrier formula, Eq. (30), is still applicable and that $T_2 \approx 1$ and $R_2 = 1 - T_2 \approx 0$ due to the Klein tunneling. Therefore, $T_{12} \approx T_1$, the role of a phase shift ϕ is negligible, and one can write — for the wave leaving the inner lead with the total angular momentum $\hbar j$ (with $j = \pm 1/2, \pm 3/2, \dots$) — the transmission probability as

$$(T_j)_{R_i \ll R_o} \approx T(u_j) = \begin{cases} \frac{2\sqrt{1-u_j^2}}{1+\sqrt{1-u_j^2}} & \text{if } |u_j| \leq 1, \\ 0 & \text{if } |u_j| > 1, \end{cases}$$

$$\text{with } u_j = \frac{j}{k_F R_i}. \quad (52)$$

Subsequently, the summation for the m -th power of T_j can be approximated (notice that we have assumed $k_F R_i \gg 1$) by integration over $-1 \leq u \leq 1$, leading to

$$\sum_j (T_j)^m \approx k_F R_i \int_{-1}^1 du [T(u)]^m = 2k_F R_i \langle T^m \rangle_u, \quad (53)$$

where, also using the symmetry $T(-u) = T(u)$, we have defined

$$\langle T^m \rangle_u = \int_0^1 du \left(\frac{2\sqrt{1-u^2}}{1+\sqrt{1-u^2}} \right)^m = \frac{\sqrt{\pi} \Gamma(m+2)}{4\Gamma(m+\frac{5}{2})} \left[2m+3 - 2m {}_2F_1 \left(\frac{1}{2}, 1; m+\frac{5}{2}; -1 \right) \right]. \quad (54)$$

The first four values of $\langle T^m \rangle_u$ are listed in Table I. Substituting the above into Eqs. (5), (12), (17), and (18), we obtain

$$\begin{aligned} G &\approx (4-\pi) G_{\text{Sharvin}}, \\ &\text{with } G_{\text{Sharvin}} = 2g_0 k_F R_i, \\ F &\approx \frac{9\pi - 28}{3(4-\pi)} \simeq 0.1065, \quad (R_i \ll R_o) \quad (55) \\ R_3 &\approx \frac{204 - 65\pi}{5(4-\pi)} \simeq -0.04742, \\ R_4 &\approx \frac{1575\pi - 4948}{21(4-\pi)} \simeq 0.0004674. \end{aligned}$$

For the Corbino disk, it is also possible to perform the analytical mode matching for the heavily-doped leads, but arbitrary disk doping k_F and radii ratio R_o/R_i [20, 67]. We skip the details of the derivation here and just give the transmission probabilities

$$T_j = \frac{16}{\pi^2 k^2 R_i R_o} \frac{1}{\left[\mathfrak{D}_j^{(+)} \right]^2 + \left[\mathfrak{D}_j^{(-)} \right]^2}, \quad (56)$$

where

$$\begin{aligned} \mathfrak{D}_j^{(\pm)} &= \text{Im} \left[H_{j-1/2}^{(1)}(k_F R_i) H_{j\mp 1/2}^{(2)}(k_F R_o) \right. \\ &\quad \left. \pm H_{j+1/2}^{(1)}(k_F R_i) H_{j\pm 1/2}^{(2)}(k_F R_o) \right], \quad (57) \end{aligned}$$

and $H_\nu^{(1)}(\rho)$ [$H_\nu^{(2)}(\rho)$] is the Hankel function of the first [second] kind. In Fig. 5, we provide the comparison between the values of the conductance and the next three charge cumulants obtained by substituting the exact T_j -s given above into Eqs. (5), (12), (17), (18), and performing the numerical summation over j with the approximate values given in Eq. (55). It is easy to see that the radii ratio of $R_o/R_i = 5$ is sufficient to reproduce our predictions for the narrow-opening limit, with good accuracy, typically starting from $k_F R_i = 50-100$. (This time the higher cumulant is considered, the faster the convergence.)

Table I: The first four cumulants for the transmission probabilities, $\langle T^m \rangle$, for different transport regimes in graphene and the corresponding values of the four charge-transfer characteristics, see Eqs. (5), (12), (17), (18).

Cumulant	Transport regime (or approximation)			
	<i>Pseudodiffusive</i> , $k_F=0, W \gg L^a$	<i>Sub-Sharvin</i> , $k_F W \gg 1^b$	$\langle X \rangle_{\rho_{\text{approx}}(T)}$, see Eq. (WW) ^c	<i>Narrow-opening</i> , $k_F R_i \gg 1, R_i \ll R_o^d$
$\langle T \rangle$	1	$\pi/4$	$\pi/4$	$4 - \pi$
$\langle T^2 \rangle$	2/3	$7\pi/32$	2/3	$40/3 - 4\pi$
$\langle T^3 \rangle$	8/15	$51\pi/256$	$3\pi/16$	$192/5 - 12\pi$
$\langle T^4 \rangle$	16/35	$759\pi/4096$	8/15	$32(332/105 - \pi)$
G/G_{Sharvin}	∞^e	$\pi/4$	$\pi/4$	$4 - \pi$
F	1/3	1/8	$1 - 8/3\pi \simeq 0.1512$	$(9\pi - 28)/3(4 - \pi)$
R_3	1/15	-1/32	$5/2 - 8/\pi \simeq -0.04648$	$(204 - 65\pi)/5(4 - \pi)$
R_4	-1/105	-5/512	$10 - 472/15\pi \simeq -0.01615$	$(1575\pi - 4948)/21(4 - \pi)$

Expressions for $\langle T^m \rangle$ with arbitrary $m \geq 1$ are given by: ^a)Eq. (38); ^b)Eqs. (46), (50); ^c)Eq. (...); ^d)Eq. (54).

^e)For $k_F = 0$, $G = g_0 W/\pi L$, with $g_0 = 4e^2/h$, coincides with $G_{\text{Sharvin}} = 0$.

III. DISTRIBUTIONS OF TRANSMISSION PROBABILITIES

A compact and intuitive representation of the charge-transfer cumulants discussed in the previous Section is provided within the distribution function of transmission probabilities $\rho(T)$. This function takes the simplest form when the transmission probability can be expressed as a monotonic function of the parameter λ , i.e., $T = T(\lambda)$. In such a case, the probability density is defined by

$$\rho(T) = \rho(\lambda) \left| \frac{d\lambda}{dT} \right|, \quad (58)$$

where $\rho(\lambda)$ is the number of transmission channels per unit of λ [here constant and determined by the appropriate quantization rule, see Eqs. (6), (24), or (52)], and $d\lambda/dT$ is the derivative of the inverse function $\lambda(T)$. In a generic situation, the right-hand side in Eq. (58) needs to be replaced by the sum over the monotonicity intervals of $T = T(\lambda)$.

In the pseudodiffusive limit, $k_F = 0$ and $W \gg L$, the transmission probability given by Eq. (34) immediately implies

$$\rho_{\text{diff}}(T) = \frac{W}{2\pi L} \frac{1}{T\sqrt{1-T}} = \frac{G_{\text{diff}}}{2\pi\sigma_0} \frac{1}{T\sqrt{1-T}}, \quad (59)$$

where we recall the pseudodiffusive conductance $G = G_{\text{diff}}$ given in Eq. (39). The distribution $\rho_{\text{diff}}(T)$ is visualized in Fig. 3(c).

Analyzing the sub-Sharvin transport, we now change the order of presentation by switching to the disk geometry to point out that in the narrow-opening limit, i.e., for $k_F R_i \gg 1$ and $R_i \ll R_o$, the transmission probability $T(u_j)$ given by Eq. (52) leads to another closed-form expression for the distribution, namely

$$\rho_{R_i \ll R_o}(T) = \frac{G_{\text{Sharvin}}}{g_0} \frac{T}{(2-T)^2 \sqrt{1-T}}, \quad (60)$$

with $G_{\text{Sharvin}} = 2g_0 k_F R_i$ for a circular lead.

In the case of parallel interfaces at a distance L , see Fig. 3(a), the description of the sub-Sharvin transport becomes more complex, since the transmission probability $T_{k_y}(E)$, see Eqs. (32) and (33), is no longer a monotonic function of k_y . The distribution $\rho(T)$ obtained numerically for $k_F L = 25$ is presented in Fig. 3(e), where the continuous k_y corresponds to the $W \gg L$ limit. It can be noticed that each of the seven transmission minima [see Fig. 3(d)] produces a distinct (integrable) singularity of $\rho(T)$ located at $0 < T_{\text{min}} < 1$. A closed-form, asymptotic expression for $\rho(T)$ in the $k_F \rightarrow \infty$ limit is missing; instead, we propose the approximation directly following from $\{T_{k_y}\}_{\text{incoh}}$ given by Eq. (41), i.e.,

$$\rho_{\text{approx}}(T) = \frac{G_{\text{Sharvin}}}{g_0} \frac{T}{\sqrt{1-T^2}}. \quad (61)$$

Subsequent approximations for the cumulants can be evaluated as

$$\langle T^m \rangle_{\rho_{\text{approx}}(T)} = \frac{g_0}{G_{\text{Sharvin}}} \int_0^1 dT T^m \rho_{\text{approx}}(T), \quad m \geq 1. \quad (62)$$

The numerical values for $m = 1, \dots, 2$ are listed in Table I, together with the corresponding approximations for the charge-transfer cumulants F , R_3 , and R_4 , which are also depicted in Figs. 4(b-d) [thick horizontal lines]. We notice that these values typically match the incoherent ones, obtained by substituting Eq. (46) into Eq. (50), within the accuracy that allows unambiguous identification of the transport regime. A surprising exception is the case of R_4 , for which the proximity of the pseudodiffusive (-1/105) and incoherent (-5/512) values is merely a coincidence. [By definition, the conductance $G \approx (\pi/4) G_{\text{Sharvin}} = (k_F W/\pi) \langle T \rangle_{\rho_{\text{approx}}(T)}$.]

The functional forms of $\rho(T)$ derived in this Section, along with a selection of others previously reported in the literature, can be found in Table II.

Table II: Basic quantum-transport regimes in selected nanoscopic systems characterized by the conductance (G), the Fano factor (F), and statistical distribution of transmission probabilities $\rho(T)$. Remaining symbols are the Fermi wavenumber k_F , the conductance quantum $g_0 = 2e^2/h$ for the two-dimensional electron gas (2DEG) or $4e^2/h$ for graphene, and the number of open channels N_{open} .

Transport regime	System	G	F	$\rho(T)$	Refs.
<i>Standard ballistic</i>	Sharvin contact in 2DEG, width W	$G_{\text{Sharvin}} = g_0 k_F W / \pi$	0	$N_{\text{open}} \delta(1 - T)$	[31, 32]
<i>(Pseudo)-diffusive</i>	diffusive conductor	$g_0 \ll G \ll G_{\text{Sharvin}}$	1/3	$\frac{G}{2g_0} \frac{1}{T\sqrt{1-T}}$	[68, 69]
	Charge-neutral graphene sample (width W , length L)	$\sigma_0 \frac{W}{L}, \sigma_0 = \frac{4e^2}{\pi h}$	1/3	$\frac{G}{2\pi\sigma_0} \frac{1}{T\sqrt{1-T}}$	[18, 19]
	Charge-neutral graphene disk (inner radii R_i , outer radii R_o)	$\frac{2\pi\sigma_0}{\ln(R_o/R_i)}$			[20]
<i>Sub-Sharvin</i>	Doped graphene sample (width W , length L)	$\frac{\pi}{4} G_{\text{Sharvin}}$	1/8	$\approx \frac{G_{\text{Sharvin}}}{g_0} \frac{T}{\sqrt{1-T^2}}$	[28], this work
	Doped graphene disk, $B = 0$ (inner radii R_i , outer radii R_o)	$\frac{\pi^a}{4} < \frac{G}{G_{\text{Sharvin}}} < 4 - \pi^c$	$1/8^a > F > 0.1065^c$	$\frac{(G_{\text{Sharvin}}/g_0) T^c}{(2-T)^2 \sqrt{1-T}}$	[29], this work
	Doped graphene disk, $B \rightarrow B_{c,2}^{-d}$	$G \rightarrow 0$	$0.5497^a < F < 1^c$	—	[35]
<i>Chaotic</i>	Symmetric cavity	$0 < G < G_{\text{Sharvin}}^e$	1/4	$\frac{2G}{\pi g_0} \frac{1}{T^{1/2} \sqrt{1-T}}$	[70]

^{a)} Reached for $R_i/R_o \rightarrow 1$. ^{b)} Defined as $G_{\text{Sharvin}} = 2g_0 k_F R_i$. ^{c)} Reached for $R_i/R_o \rightarrow 0$.

^{d)} Magnetic field corresponding to the vanishing conductance, $B_{c,2} = 2(\hbar/e)k_F/(R_o - R_i)$.

^{e)} Defined via the opening width w ; i.e., $G_{\text{Sharvin}} = g_0 k_F w / \pi$.

IV. RESULTS AND DISCUSSION

In this Section, we confront the predictions from analytical theory for the charge-transfer cumulants (see Sec. II) with the results of computer simulations of electron transport in selected nanostructures in graphene shown in Fig. 1 (for the parameters, see Table III). Since discrete structures carved out of a honeycomb lattice exhibit Fabry-Pérot type oscillations in all studied transport properties as a function of Fermi energy, and (typically) the higher the cumulant, the larger the oscillation magnitude, we limit the forthcoming discussion to the Landauer-Büttiker conductance (G) and the Fano factor (F). It is also worth noting that the ratio of the former to the Sharvin conductance (G/G_{Sharvin}) accompanied by F provides sufficient information to unambiguously identify one of the basic quantum transport regimes, see Table II, if applica-

A. Tight-binding Hamiltonian

This part of the analysis starts from the tight-binding model of graphene, with Hamiltonian

$$H = \sum_{i,j,s} t_{ij} c_{i,s}^\dagger c_{j,s} + \sum_{i,s} V_i n_{i,s}, \quad (63)$$

where the indices i, j run over sites in the honeycomb lattice of carbon atoms, and $s = \uparrow, \downarrow$ is the spin up/down orientation. The hopping-matrix elements are given by

$$t_{ij} = \begin{cases} -t_0 & \text{if } i, j \text{ are nearest-neighbors,} \\ 0 & \text{otherwise,} \end{cases} \quad (64)$$

with $t_0 = 2.7$ eV. For the systems shown in Figs. 1(a), 1(d), and 1(e), the electrostatic potential energy $V_j = V(x_j)$ varies only along the main axis. It equals $-V_{\text{infty}}$, with $V_{\text{infty}} = t_0/2 = 1.35$ eV, in the leads and raise to $V_j = 0$ in the sample

Table III: Detailed parameters of the systems studied numerically (see also Fig. 1). For each case, the main spatial dimension is also given in physical units.

System	Defining parameters	System (sample) length, L_{tot} (L') ^{a)}	No. of sites ^{b)}
<i>Constriction with zigzag edges</i>	$W_{\infty} = 210\sqrt{3}a$	$254a \simeq 62.5 \text{ nm}$	105, 452
	$W = 60\sqrt{3}a, L = 104a$	($\equiv L$)	(24, 960)
<i>Half-Corbino disk</i>	$W_{\infty} = 700a$	$120\sqrt{3}a \simeq 51.1 \text{ nm}$	336, 000
	$R_2 = 4R_1 = 200a$	($\equiv R_2 - R_1$)	(136, 035)
<i>Circular quantum dot</i>	$W_{\infty} = 210\sqrt{3}a, R = 105\sqrt{3}a$	$512a \simeq 126 \text{ nm}$	320, 881
	$w = 60\sqrt{3}a$	($362a$)	(240, 389)
<i>Circular quantum dot with a circular hole</i>	$W_{\infty} = 210\sqrt{3}a, R = 105\sqrt{3}a$	$512a \simeq 126 \text{ nm}$	301, 148
	$w = 60\sqrt{3}a, r = 30\sqrt{3}a$	($362a$)	(220, 656)

^{a)} L_{tot} —the distance between semi-infinite leads; L' —the distance between interfaces (given in parenthesis).

^{b)} Total no. of sites between the leads. (No. of sites with $V(x) > -V_{\infty}/2$ is given in parenthesis.)

area. The abrupt potential increase at the sample-lead interface is smoothed over the length L_s , according to the function

$$\Theta_{L_s}(x) = \begin{cases} 0 & \text{if } x < -L_s/2, \\ \frac{1}{2} + \frac{1}{2} \sin(\pi x/L_s) & \text{if } |x| \leq L_s/2, \\ 1 & \text{if } x > L_s/2. \end{cases} \quad (65)$$

The potential barrier, composed of two steps at $x = x_1$ and $x = x_2 \equiv x_1 + L$, namely

$$V(x) = V_{\infty} [\Theta_{L_s}(x - x_1) - \Theta_{L_s}(x - x_2)] - V_{\infty}, \quad (66)$$

is rectangular for $L_s = 0$ [solid line in Fig. 1(b)], whereas it has a sinusoidal shape for $L_s = L$ [dashed line]. For the half-disk shown in Fig. 1(c), we simply take $V_j = V(r_j)$, where r_j is the radius in polar coordinates, with the same function $V(r)$ as in Eq. (66). The interface positions (x_1, x_2) coincide with the ends of the central (narrowest) part with parallel edges [see Fig. 1(a)], the inner/outer disk radii [Fig. 1(c)], or with the neckings limiting the dot region [Fig. 1(d,e)]. The remaining symbols in Eq. (63) are a creation (annihilation) operator for electron with spin s at lattice site i , $c_{i,s}^{\dagger}$ ($c_{i,s}$) and the particle-number operator $n_{i,s} = c_{i,s}^{\dagger} c_{i,s}$. (Since the Hamiltonian (63) can be represented as the sum of the two commuting terms, one for $s = \uparrow$ and the other for $s = \downarrow$, it is sufficient to calculate the transport characteristics for one spin direction and to multiply the results by the degeneracy factor 2.)

In the following, we consider $0 \leq L_s \leq L$ only for the constriction shown in Fig. 1(a); once the effect of the smooth potential barrier is identified, the discussion of the remaining systems concentrates on the case of $L_s = 0$ (i.e., abrupt step).

B. Constriction with zigzag edges

As a first example of the system, for which the analytical mode matching technique presented in Sec. II cannot be directly applied, we consider the constriction with zigzag edges,

earlier considered as the valley [71] or spin [72, 73] filter, depicted in Fig. 1(a). The central section of this system is an almost perfect square, with the length $L = 104a \simeq 25.58 \text{ nm}$ and the width $W = 60\sqrt{3}a \simeq 25.57 \text{ nm}$ (see also Table III), attached to wedge-shaped electrodes that evolve into wide stripes with the width $W_{\text{infy}} = 210\sqrt{3}a \simeq 89.5 \text{ nm}$. Such a geometry is chosen to mimic the typical experimental situation, in which the nanostructure in graphene is contacted by much wider metallic leads [74]. Also, the potential step height, $V_{\infty} = t_0/2 \simeq 1.35 \text{ eV}$ is not far from the results of some first-principles calculations for graphene-metal structures [75, 76]. Semi-infinite leads of a constant width W_{∞} play a role of the waveguides shown in Fig. 2; they can be divided into the repeating supercells in order to find the propagating modes numerically, by adapting the scheme developed by Ando for a square lattice [77] to the honeycomb lattice. For the potential profile given by Eqs. (65) and (66), the number of propagating modes (per one direction) is equal in the left and right leads, $N_L = N_R$ [78].

Since the central section of the system is bounded by two parallel interfaces separating weakly and heavily doped regions, one can expect that the key findings for a graphene strip in the sub-Sharvin regime, see Eqs. (44) and (51) still apply, at least for $L_s \ll L$. However, the system width now varies with the position along the main axis, so the scattering cannot be described independently for each normal mode, as in Eq. (27). Instead, the mode mixing occurs, and — if scattering from the left is considered — we can define the transmission matrix $\mathbf{t} = (t_{mn})$, with $m = 1, \dots, N_R$ and $n = 1, \dots, N_L$, and the reflection matrix $\mathbf{r} = (r_{mn})$, with $m = 1, \dots, N_L$, $n = 1, \dots, N_L$. The details of the calculations are presented in Appendix A; here we only mention that Eqs. (5) and (12) for measurable quantities remain valid, provided that the transmission probabilities T_n are defined as eigenvalues of the matrix $\mathbf{t}\mathbf{t}^{\dagger}$. Alternatively, one can express the Landauer-Büttiker conductance and the Fano factor in the

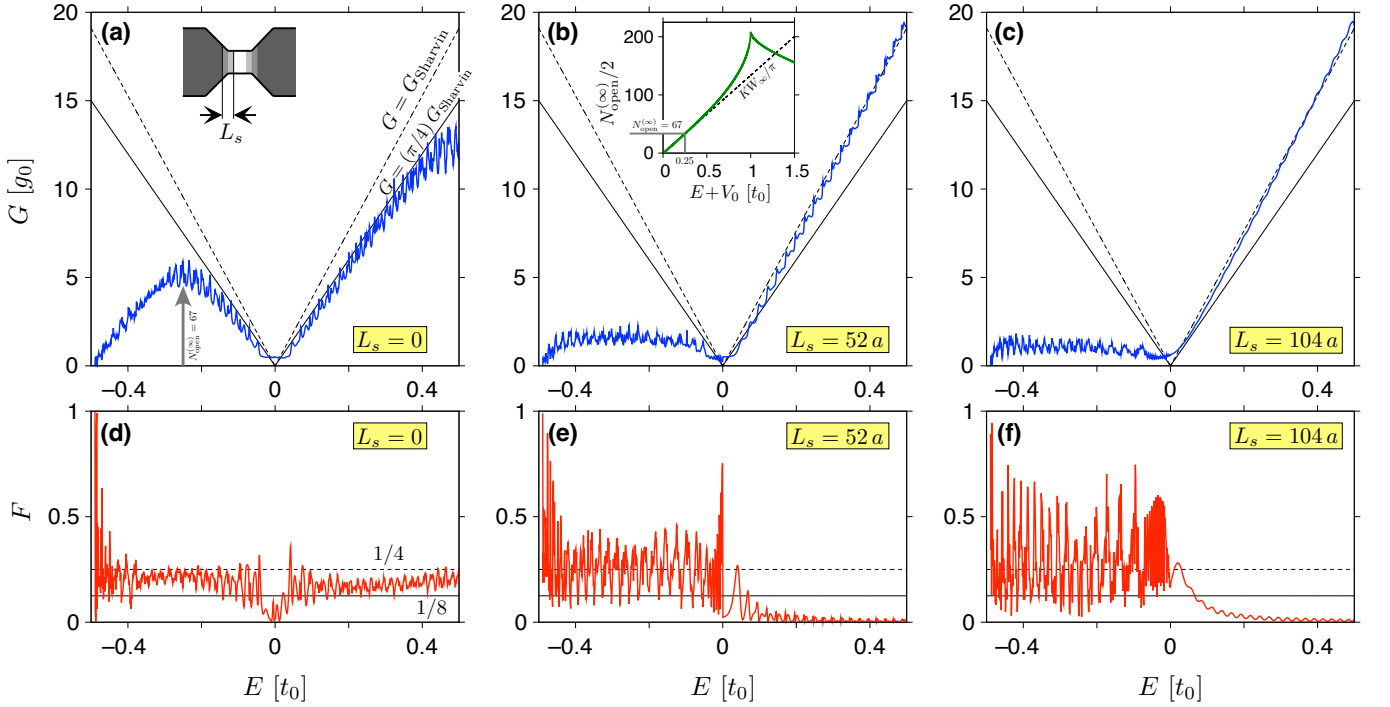


Figure 6: Conductance in the units of $g_0 = 4e^4/h$ (a–c) and the Fano factor (d–f) for the constriction with zigzag edges, see Fig. 1(a), displayed as functions of the Fermi energy defined with respect to the top as the electrostatic potential barrier in the narrow region, see also Fig. 1(b). The subsequent panels correspond to abrupt ($L_s = 0$), partly-smooth ($L_s = L/2 = 52a$), and fully-smooth ($L_s = L = 104a$) potential steps. Numerical results following from the tight-binding calculations are depicted with thick lines. Thin solid lines mark the sub-Sharvin values given by Eqs. (44), (51); dashed lines in (a–c) mark the Sharvin conductance given by Eq. (8) or, in (d–f), the shot-noise power characterizing symmetric cavity, $F = 1/4$. (The constriction width is $W = 60\sqrt{3}a$; for the remaining simulation details, see Table III.) Inset in (b) presents the number of propagating modes in the leads versus the energy $E + V_0$, with the step height $V_0 = t_0/2 = 1.35eV$.

basis-independent form, referring to the traces of the matrices tt^\dagger and $(tt^\dagger)^2$, namely

$$G = \frac{2e^2}{h} \text{Tr}(tt^\dagger), \quad (67)$$

$$F = 1 - \frac{\text{Tr}(tt^\dagger)^2}{\text{Tr}(tt^\dagger)}. \quad (68)$$

The factor 2 in Eq. (67) denotes the spin degeneracy. The valley degeneracy of the transmission eigenvalues is now only approximate, since the dispersion relation following from the Hamiltonian (63) is no longer perfectly conical, but shows the trigonal warping [15]. (For zigzag edges and electron doping, exact valley degeneracy occurs for all but one mode; for armchair edges the degeneracy is approximate for all modes [79, 80].)

The results of our computer simulations are depicted by the thick colored lines in Fig. 6. They match the sub-Sharvin values (marked by black solid lines) for electron doping ($E > 0$) and the abrupt potential step ($L_s = 0$). For hole doping ($E < 0$) and $L_s = 0$ the conductance G is still close to $(\pi/4)G_{\text{Sharvin}}$ as long as the number of propagating modes in the leads is sufficiently large [see the inset in Fig. 6(b)]. At the same time, the Fano factor is rather closer to the value of $F = 1/4$, which characterizes the symmetric cavity. In contrast, for smooth barriers ($L_s \gg a$) we have $G \approx G_{\text{Sharvin}}$ for

$E > 0$ and $G \ll G_{\text{Sharvin}}$ for $E < 0$ (the conductance suppression due to the presence of two p-n junctions), as can be expected for the standard (i.e., Schrödinger) ballistic system. At the same time, the Fano factor switches from $F \ll 1$ (for $E > 0$) to $F \approx 1/4$ (for $E < 0$). These findings are consistent with the results for smooth potential barriers and a strip with parallel edges, with mass confinement, presented in Ref. [28].

We see then that the constriction with zigzag edges carved out of a honeycomb lattice preserves all the key features of the idealized Dirac system studied previously.

C. Half-disk and circular quantum dots

We now focus on the case of abrupt potential step ($L_s = 0$) and consider the geometries for which the possible role of the edges is reduced (the half-Corbino disk) or amplified (circular quantum dot, without- or with a circular hole) compared to the constriction discussed above. The conductance and the Fano factor determined from Eqs. (67) and (68) after numerical calculation of the corresponding transmission matrix (see also Appendix A) are presented in Fig. 7.

In the half-disk case, see Figs. 7(a) and 7(d), the conductance (for $E > 0$) remains in the interval $G_{\text{Sharvin}} \gtrsim G \gtrsim (4 - \pi)G_{\text{Sharvin}}$ (notice that the radii ratio is $R_2/R_1 = 4$, and

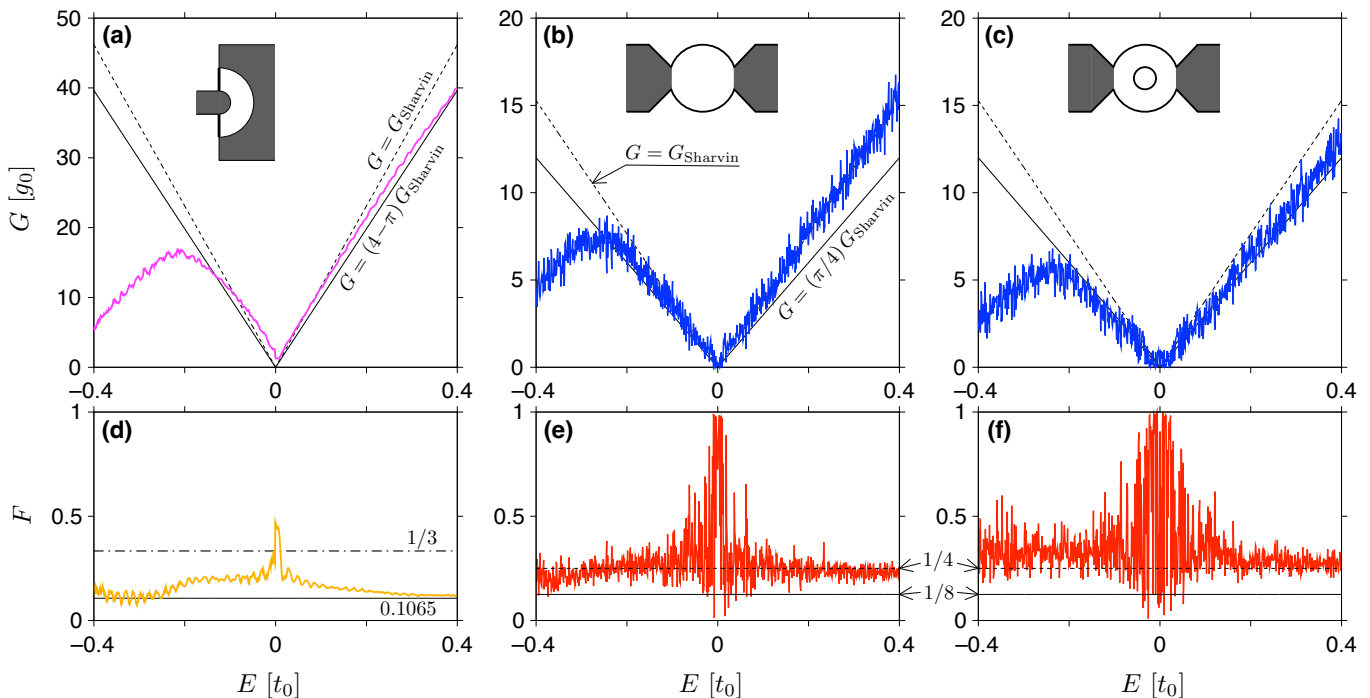


Figure 7: Same as in Fig. 6, but for the half-Corbino disk (a,d) [see also Fig. 1(c)], circular quantum dot (b,e) [see Fig. 1(d)], and circular quantum dot with a circular hole (c,f) [see Fig. 1(e)]. Thin solid lines in (a) and (d) show the results given in Eq. (55) for the narrow-opening limit; dash-dotted line in (d) marks the pseudodiffusive shot-noise power, $F = 1/3$. Remaining lines are same as in Fig. 6. (Other simulation details are given in Table III.

thus the relevant analytic approximations are given in Eq. (55) for the narrow-opening limit), with a tendency to approach the narrow-opening value with increasing E . For $E < 0$, the conductance behavior is less clear, but the values of G are still close to both G_{Sharvin} and $(4 - \pi)G_{\text{Sharvin}}$. In contrast, the Fano factor is close to the narrow-opening value of $F \approx 0.1065$ for both $E > 0$ and $E < 0$, except in the small vicinity of the charge-neutrality point ($E = 0$), where it is noticeably closer to the pseudodiffusive value of $F = 1/3$.

For circular quantum dots Fabry-Pérot interference combined with scattering from irregular sample edges leads to much more pronounced oscillations of both G and F , discussed as functions of the Fermi energy, than in the case of a half-Corbino disk. In addition, the spectra presented in Figs. 7(b,c) for G and 7(e,f) for F suggest that the first charge-transfer characteristic (G), discussed in isolation, may lead to the misidentification of the Sharvin or sub-Sharvin transport regime. Looking at the F spectra, it is clear that the chaotic cavity (with $F = 1/4$) is the closest of the simple models that captures key features of the circular quantum dot (both in the variant without- or with a hole), at least for higher electron or hole dopings. The conductance itself, related to the Sharvin value for $E > 0$, appears to be misleadingly close to G_{Sharvin} in the absence of a hole, or to $(\pi/4)G_{\text{Sharvin}}$ in the presence of a hole. (For $E < 0$, the suppression of G due to p-n junctions occurs in both cases.)

Therefore, complex nanostructures with irregular edges may accidentally show some features of Sharvin (or sub-Sharvin) transport, but systematic discussion of quantum

transport unveils the chaotic nature of the system.

V. CONCLUSIONS

We have presented the analytical technique that allows one to calculate arbitrary charge transfer cumulant for doped graphene sample in two distinct physical situations: (i) two long and parallel abrupt interfaces separate the sample and the leads; (ii) a narrow circular interface governs transport through the much wider sample toward an external lead. In both cases, compact expressions are available for sufficiently high sample doping (infinite doping is assumed for the leads), for which multiple scattering between the interfaces can be taken into account, imposing the random phase each time the electron passes the sample area.

We have also reviewed the most common quantum transport regimes described in the literature, with their statistical distributions of transmission probabilities. Evidence for a novel *sub-Sharvin* transport regime in doped graphene is pointed out.

Next, the results of analytical considerations for idealized systems are compared with computer simulations of quantum transport for more realistic systems carved out of a honeycomb lattice. The effects of finite doping in the leads, smooth potential steps, trigonal warping, and irregular sample edges are included in our simulations. The results show that the main features of the analytical approach discussed in the first part, which defines the sub-Sharvin transport regime

in graphene (with its variants for parallel interfaces and for the narrow-opening limit), are well reproduced in discrete systems on a honeycomb lattice, provided that the sample edges are straight and relatively short; i.e., with a total length comparable to or shorter than the total length of the sample-lead interfaces. In contrast, for systems with long and irregular edges, different charge-transfer cumulants may suggest different quantum transport regimes, making unambiguous classification difficult or impossible.

Although our paper focuses on graphene, we expect that the main effects will also occur in other two-dimensional crystals such as silicene, germanene, or stanene [81, 82]. This prediction is based on the nature of the results presented, in particular the fact that the occurrence of the sub-Sharvin transport regime is related to the conical dispersion relation rather than to the transmission via evanescent waves, which is responsible for the graphene-specific phenomena that occur at the charge neutrality point.

Acknowledgements

The work was mainly completed during a sabbatical granted by the Jagiellonian University in the summer semester of 2023/24. We gratefully acknowledge Polish high-performance computing infrastructure PLGrid (HPC Center: ACK Cyfronet AGH) for providing computer facilities and support within computational grant no. PLG/2024/017208.

Appendix A: Numerical mode-matching for the honeycomb lattice

1. The nanosystem

In the following, we show how the computational method originally developed by Ando for a square lattice [77] can be adapted to the honeycomb lattice. The key point is to notice that — when discussed on the level of tight-binding Hamiltonian (63) — a honeycomb lattice with nearest-neighbor hoppings only becomes equivalent to a square lattice with some bonds removed (see Fig. 8(a)). The reasoning presented here can, with simple modifications, be applied to a honeycomb, square, or even triangular lattice (the last case may be applicable when discussing the recently discovered two-dimensional form of gold, *goldenene*, see Ref. [83]).

The nanosystem, shown schematically in Fig. 8(b), represents a generic case that is tractable within the Landauer-Büttiker formalism. Two semi-infinite leads are built from repeatable sections, allowing one to find the normal modes (propagating and evanescent) that define the basis for the scattering matrix — with moderate computational effort — via the secular equation (see next subsection); the central part may have an arbitrary shape, and thus the mode matching must be performed numerically on the lattice, which reduces to solving a sparse linear system of equations.

The details (and remaining assumptions) of both computational steps are given below.

2. Solutions in the leads

Keeping in mind the analogy between the honeycomb lattice and the square lattice mentioned above, we now consider an infinitely long wire with a width of N sites, short sections of which are schematically shown in Figs. 8(b) (for zigzag edges) and 8(c) (for armchair edges). Quantum-mechanical equation of motion can be written as

$$T^\dagger \varphi_{j-1} + H_0 \varphi_j + T \varphi_{j+1} = E \varphi_j, \quad (\text{A1})$$

where

$$\varphi_j = \begin{pmatrix} \varphi_{A,j} \\ \varphi_{B,j} \end{pmatrix} \quad (\text{A2})$$

is the $2N$ -component wavefunction with the probability amplitudes corresponding to the sites in the A and B blocks; i.e., $\varphi_{A(B),j} = [\varphi_{A(B),j}^{(1)}, \dots, \varphi_{A(B),j}^{(N)}]^T$. It is worth noting that the lead width in physical units, W_∞ , is related to N as follows

$$W_\infty = Na \times \begin{cases} \frac{1}{2}\sqrt{3} & (\text{zigzag edges}), \\ 1 & (\text{armchair edges}). \end{cases} \quad (\text{A3})$$

Therefore, W_∞ can be interpreted as a circumference of a nanotube that can be created by connecting the edge sites at each section by additional (vertical) hopping.

For *zigzag edges*, H_0 and T are $2N \times 2N$ matrices with the following block structure

$$H_0^{(\text{zig})} = \begin{pmatrix} H_A^z & P \\ P^\dagger & H_B^z \end{pmatrix}, \quad T^{(\text{zig})} = \begin{pmatrix} 0 & 0 \\ P' & 0 \end{pmatrix}. \quad (\text{A4})$$

The block matrices $H_A^z \neq H_B^z$ contain values of the electrostatic potential energy (i.e., $-V_0$ for all sites) and *vertical* hopping elements depicted in Fig. 8; they are tridiagonal matrices with every second hopping removed, namely

$$\begin{aligned} (H_A^z)_{ll'} &= -V_0 \delta_{l,l'} - t_0 (\delta_{l,l'-1} + \delta_{l-1,l'}) [(l \bmod 2)], \\ (H_B^z)_{ll'} &= -V_0 \delta_{l,l'} - t_0 (\delta_{l,l'-1} + \delta_{l-1,l'}) [(l+1) \bmod 2], \end{aligned} \quad (\text{A5})$$

where $l, l' = 1 \dots N$, and $\delta_{ll'}$ is the Kronecker delta. The matrices P and P' contain horizontal hoppings; for zero magnetic field, we have

$$(P)_{ll'} = (P')_{ll'} = -t_0 \delta_{l,l'}. \quad (\text{A7})$$

For a uniform magnetic field, the Peierls substitution can be applied; it reads $P_{ll} \rightarrow P_{ll} \exp(2\pi i l \Phi_a / \Phi_0)$ ($l = 1 \dots N$), with Φ_a the flux per unit cell and $\Phi_0 = h/e$ the flux quantum. (The generalization for some geometric strains, leading to position-dependent hopping is also possible, provided that the invariance upon $j \rightarrow j+1$, see Eq. (A1), is preserved.)

For *armchair edges*, the site-numbering scheme presented in Fig. 8(c) allows us to keep the block structure of Eq. (A1), with

$$H_0^{(\text{arm})} = \begin{pmatrix} H_A^a & T_y \\ T_y^\dagger & H_B^a \end{pmatrix}, \quad T^{(\text{arm})} = \begin{pmatrix} 0 & 0 \\ T_x & 0 \end{pmatrix}. \quad (\text{A8})$$

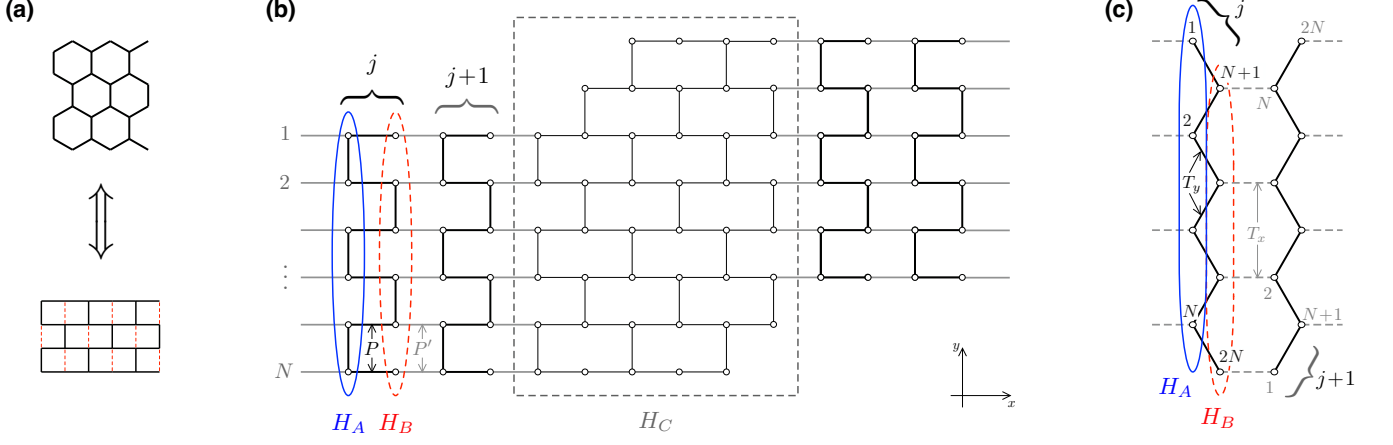


Figure 8: (a) A nanosystem of 24 sites carved out of the honeycomb lattice and an equivalent section of a square lattice with every second vertical bond removed (red dashed lines). (b) Schematic of an *open* system in computer simulation. Semi-infinite leads (with zigzag edges) are built from identical sections (the j -th and $j+1$ sections are marked for the left lead), each consisting of two subsections A and B , coupled only by horizontal bonds contributing to the matrix blocks P and P' . Leads contact the central section (surrounded by dashed rectangle) of a generic shape. (c) Analogous decomposition and the numbering scheme for the lead with *armchair* edges. [See main text for details.]

Now, the matrices $H_A^a = H_B^a$ contain only diagonal elements,

$$(H_A^a)_{ll'} = (H_B^a)_{ll'} = -V_0 \delta_{l,l'}. \quad (\text{A9})$$

The remaining blocks, T_x and T_y , are given by

$$(T_x)_{ll'} = -t_0 \delta_{l, N-l'+1} \quad (\text{A10})$$

$$(T_y)_{ll'} = -t_0 (\delta_{l,l'} + \delta_{l-1,l'}), \quad (\text{A11})$$

where $l, l' = 1 \dots N$ again.

Using the familiar Bloch ansatz,

$$\varphi_j = \lambda^j \varphi_0, \quad (\text{A12})$$

we arrive to the secular equation, for zigzag edges,

$$\begin{pmatrix} H_A^z - E \mathbb{I} & P \\ P' & 0 \end{pmatrix}^{-1} \begin{pmatrix} 0 & -P'^{\dagger} \\ -P^{\dagger} & E \mathbb{I} - H_B^z \end{pmatrix} \varphi_0 = \lambda \varphi_0, \quad (\text{A13})$$

where \mathbb{I} is the $N \times N$ identity matrix and the eigenvalues λ are complex with $|\lambda| = 1$ (for *propagating modes*) or real with $|\lambda| \neq 1$ (for *evanescent modes*). For armchair edges, Eq. A13 holds with the following substitutions

$$H_A^z \rightarrow H_A^a, \quad H_B^z \rightarrow H_B^a, \quad P \rightarrow T_y, \quad P' \rightarrow T_x. \quad (\text{A14})$$

(If the generalization involving the dependence of the matrix elements on the position across the lead, such as the Peierls substitution mentioned above, is desired, one must double the number blocks in Eq. (A8) by introducing $\varphi_j = (\varphi_{A1,j}, \varphi_{B1,j}, \varphi_{A2,j}, \varphi_{B2,j})^T$; however, such a case is beyond the scope of the present paper).

3. Basis for the scattering matrix

The secular equation derived above, given explicitly by Eq. (A13) for zigzag edges (z.e.), with the necessary substitutions for armchair edges (a.e.) in Eq. (A14), can be diagonalized numerically using standard software packages in order to

find the full set of eigenvalues (λ) with corresponding right-eigenvectors $\varphi_0^{(\lambda)}$. We chose the double precision LAPACK routines `dgemm` and `dgeev`, see Ref. [84].

To correctly define the scattering matrix, the propagating modes must be normalized so that they carry equal currents along the main axis of each lead (i.e., the x -axis direction in Fig. 8).

In general, the total current incoming at the i -th lattice site of the system described by the tight-binding Hamiltonian, see Eqs. (63) and (64) in the main text, is given by the time derivative of the charge,

$$\dot{n}_i = i[H, n_i] = i \sum_{j(s)} \left(t_{ij} c_i^{\dagger} c_j - t_{ij}^* c_j^{\dagger} c_i \right), \quad (\text{A15})$$

where $j(i)$ runs over the nearest neighbors of i , complex hopping (i.e., $t_{ij} \neq t_{ij}^*$) is allowed, and the spin is omitted for clarity. In turn, the current flowing from site i to site j is described by the quantum-mechanical operator

$$J_{ij} = i \left(t_{ij} c_i^{\dagger} c_j - t_{ij}^* c_j^{\dagger} c_i \right). \quad (\text{A16})$$

Taking into account all the currents incoming and outgoing from a repeatable section (j) of the lead (see Fig. 8) via individual bonds, projected onto the x -direction, bring us to the total x -current operator J_x , which — when acting on the right-eigenvector $\varphi_0^{(\lambda)}$, see Eqs. (A13) and (A14), corresponding to the eigenvalue λ — is equivalent to

$$J_x^{(\lambda)} = i \begin{pmatrix} 0 & -\lambda^{-1} P'^{\dagger} \\ \lambda P' & 0 \end{pmatrix} \quad (\text{z.e.}), \quad (\text{A17})$$

or

$$J_x^{(\lambda)} = i \begin{pmatrix} 0 & -\lambda^{-1} T_x^{\dagger} \\ \lambda T_x & 0 \end{pmatrix} \quad (\text{a.e.}). \quad (\text{A18})$$

Subsequently, the normalized eigenvector can be written as

$$\mathbf{v}_\lambda^{\text{pro}} = \frac{1}{\sqrt{|\varphi_0^{(\lambda)\dagger} J_x^{(\lambda)} \varphi_0^{(\lambda)}|}} \varphi_0^{(\lambda)} \quad (\text{for } |\lambda| = 1), \quad (\text{A19})$$

and the sign

$$s_\lambda \equiv (\mathbf{v}_\lambda^{\text{pro}})^\dagger J_x^{(\lambda)} \mathbf{v}_\lambda^{\text{pro}} = \pm 1 \quad (\text{A20})$$

identifies the direction of propagation. For evanescent modes, the normalization is irrelevant, and we simply set

$$\mathbf{v}_\lambda^{\text{eva}} = \varphi_0^{(\lambda)} \quad (\text{for } |\lambda| \neq 1). \quad (\text{A21})$$

In analogy to propagating modes, $|\lambda| > 1$ now identifies the evanescent mode decaying to the left, while $|\lambda| < 1$ identifies the evanescent mode decaying to the right. The real-space components of the normalized eigenvector for the j -th section of the lead can be written as column vectors of the dimension $2N$, namely

$$\mathbf{v}_{\lambda,j}^{\text{pro}} = \lambda^j \mathbf{v}_{\lambda,j}^{\text{pro}}, \quad \mathbf{v}_{\lambda,j}^{\text{eva}} = \lambda^j \mathbf{v}_{\lambda,j}^{\text{eva}}. \quad (\text{A22})$$

Now it is worth generalizing the discussion a bit by allowing that the left and right leads are not necessarily identical, i.e., may have different numbers of sites across, $N^{(L)}$ and $N^{(R)}$, or different electrostatic potential energy levels, $-V_0^L$ and $-V_0^R$. In such a case, the secular equation, Eq. A13, appears in the two versions, with the block matrices replaced by

$$H_A \rightarrow H_A^\alpha, \quad H_B \rightarrow H_B^\alpha, \quad P \rightarrow P_\alpha, \quad P' \rightarrow P'_\alpha, \\ \text{for } \alpha = L, R, \quad (\text{A23})$$

leading to (*a priori*) different numbers of propagating modes per single direction, $N_{\text{pro}}^{(L)}$ and $N_{\text{pro}}^{(R)}$. The number of left- (or right-) decaying evanescent modes is then given by

$$N_{\text{eva}}^{(\alpha)} = N^{(\alpha)} - N_{\text{pro}}^{(\alpha)}, \quad \text{for } \alpha = L, R. \quad (\text{A24})$$

Therefore, the number of elements (i.e., normalized eigenvectors) for the following four sets of (left-, right-) propagating and (left-, right-) decaying modes in a single electrode are as follows

$$\# \left\{ \mathbf{v}_{\lambda,j}^{\alpha,\text{pro}}, s_\lambda > 0 \right\} = \# \left\{ \mathbf{v}_{\lambda,j}^{\alpha,\text{pro}}, s_\lambda < 0 \right\} = N_{\text{pro}}^{(\alpha)}, \quad (\text{A25})$$

$$\# \left\{ \mathbf{v}_{\lambda,j}^{\alpha,\text{eva}}, |\lambda| > 1 \right\} = \# \left\{ \mathbf{v}_{\lambda,j}^{\alpha,\text{eva}}, |\lambda| < 1 \right\} = N^{(\alpha)} - N_{\text{pro}}^{(\alpha)}, \quad (\text{A26})$$

for $\alpha = L, R$.

For further considerations, we define the matrices $W_j^{(L)}$ and $W_j^{(R)}$, in which the selected eigenvectors are stored column by column, i.e.,

$$W_j^{(L)} = \begin{pmatrix} W_{A,j}^{(L)} \\ W_{B,j}^{(L)} \end{pmatrix} = \left(\left\{ \mathbf{v}_{\lambda,j}^{L,\text{pro}}, s_\lambda > 0 \right\}; \left\{ \mathbf{v}_{\lambda,j}^{L,\text{pro}}, s_\lambda < 0 \right\}; \left\{ \mathbf{v}_{\lambda,j}^{L,\text{eva}}, |\lambda| > 1 \right\} \right) \equiv \begin{pmatrix} V_{A,j}^{(L)} & U_{A,j}^{(L)} \\ V_{B,j}^{(L)} & U_{A,j}^{(L)} \end{pmatrix}, \quad (\text{A27})$$

and

$$W_j^{(R)} = \begin{pmatrix} W_{A,j}^{(R)} \\ W_{B,j}^{(R)} \end{pmatrix} = \left(\left\{ \mathbf{v}_{\lambda,j}^{R,\text{eva}}, |\lambda| < 1 \right\}; \left\{ \mathbf{v}_{\lambda,j}^{R,\text{pro}}, s_\lambda > 0 \right\}; \left\{ \mathbf{v}_{\lambda,j}^{R,\text{pro}}, s_\lambda < 0 \right\} \right) \equiv \begin{pmatrix} U_{A,j}^{(R)} & V_{A,j}^{(R)} \\ U_{B,j}^{(R)} & V_{A,j}^{(R)} \end{pmatrix}. \quad (\text{A28})$$

In the above, the blocks $W_{A,j}^{(\alpha)}$ and $W_{B,j}^{(\alpha)}$ store the matrix rows $1 \dots N^{(\alpha)}$ and $N^{(\alpha)} + 1 \dots 2N^{(\alpha)}$ (respectively), for $\alpha = L, R$. These blocks correspond to the first $N^{(\alpha)}$ sites ($W_{A,j}^{(\alpha)}$), and to the next $N^{(\alpha)}$ sites ($W_{B,j}^{(\alpha)}$) in the j -th section of a single lead.

Now, the real-space components of an arbitrary wavefunction in the j -th section of the (left,right) lead can be repre-

sented as

$$\Psi_j^{(L)} = W_j^{(L)} \left(\left\{ a_{\lambda,+}^{L,\text{pro}} \right\}; \left\{ b_{\lambda,-}^{L,\text{pro}} \right\}; \left\{ b_{\lambda,-}^{L,\text{eva}} \right\} \right)^T, \quad (\text{A29})$$

$$\Psi_j^{(R)} = W_j^{(R)} \left(\left\{ b_{\lambda,+}^{R,\text{eva}} \right\}; \left\{ b_{\lambda,+}^{R,\text{pro}} \right\}; \left\{ a_{\lambda,-}^{R,\text{pro}} \right\} \right)^T, \quad (\text{A30})$$

where each set of complex coefficients, $\left\{ a_{\lambda,+}^{L,\text{pro}} \right\}$, etc., corresponds to the matching set of eigenvectors in the matrix $W_j^{(L)}$ or $W_j^{(R)}$. Parts of the matrices $W_j^{(\alpha)}$, $\alpha = L, R$, containing

the columns corresponding to the coefficients $b_{\lambda,\mp}^{\alpha,\text{pro}}$, $b_{\lambda,\mp}^{\alpha,\text{eva}}$, read

$$\begin{pmatrix} U_{A,j}^{(L)} \\ U_{B,j}^{(L)} \end{pmatrix} = \left(\left\{ \mathbf{v}_{\lambda,j}^{L,\text{pro}}, s_\lambda < 0 \right\}; \left\{ \mathbf{v}_{\lambda,j}^{L,\text{eva}}, |\lambda| > 1 \right\} \right), \quad (\text{A31})$$

$$\begin{pmatrix} U_{A,j}^{(R)} \\ U_{B,j}^{(R)} \end{pmatrix} = \left(\left\{ \mathbf{v}_{\lambda,j}^{R,\text{eva}}, |\lambda| < 1 \right\}; \left\{ \mathbf{v}_{\lambda,j}^{R,\text{pro}}, s_\lambda > 0 \right\} \right), \quad (\text{A32})$$

where each of the blocks $U_{A,j}^{(\alpha)}$, $U_{B,j}^{(\alpha)}$ is a square matrix of dimension $N^{(\alpha)} \times N^{(\alpha)}$. The remaining columns, corresponding to the coefficients $a_{\lambda,\pm}^{\alpha,\text{pro}}$, define the matrices

$$\begin{pmatrix} V_{A,j}^{(L)} \\ V_{B,j}^{(L)} \end{pmatrix} = \left(\left\{ \mathbf{v}_{\lambda,j}^{L,\text{pro}}, s_\lambda > 0 \right\} \right), \quad (\text{A33})$$

$$\begin{pmatrix} V_{A,j}^{(R)} \\ V_{B,j}^{(R)} \end{pmatrix} = \left(\left\{ \mathbf{v}_{\lambda,j}^{R,\text{pro}}, s_\lambda < 0 \right\} \right), \quad (\text{A34})$$

where the dimensions of the blocks $V_{A,j}^{(\alpha)}$, $V_{B,j}^{(\alpha)}$ are $N^{(\alpha)} \times N_{\text{pro}}^{(\alpha)}$, for $\alpha = L, R$.

4. The scattering problem

In the last part of this Appendix, we will use the notation relevant for the leads with zigzag edges (see Fig. 8). Nevertheless, if a version of the approach for the leads with armhair edges is desired, it can be easily generated by performing the substitutions given by Eq. A14. (We emphasize here that the central section of the system, described by the tight-binding Hamiltonian H_C , may have an arbitrary shape, so that the irregular edges in the central section are also tractable within the presented approach.)

Using the definitions introduced in the previous subsections, we can now write down the quantum-mechanical equation of motion for the entire nanosystem as follows

$$\begin{pmatrix} P_L^\dagger W_{A,-1}^{(L)} + (H_B^L - E)W_{B,-1}^{(L)} & \vec{P}_L \\ \overleftarrow{P}_L^\dagger W_{B,-1}^{(L)} & \\ & H_C - E \\ & \overleftarrow{P}_R^\dagger W_{A,1}^{(R)} \\ & (H_A^R - E)W_{A,1}^{(R)} + P_R W_{B,1}^{(R)} \end{pmatrix} \begin{pmatrix} \left\{ a_{\lambda,+}^{L,\text{pro}} \right\} \\ \left\{ b_{\lambda,-}^{L,\text{pro}} \right\} \\ \left\{ b_{\lambda,-}^{L,\text{eva}} \right\} \\ \Psi_C \\ \left\{ b_{\lambda,+}^{R,\text{eva}} \right\} \\ \left\{ b_{\lambda,+}^{R,\text{pro}} \right\} \\ \left\{ a_{\lambda,-}^{R,\text{pro}} \right\} \end{pmatrix} = 0, \quad (\text{A35})$$

where we set $j = -1$ for the terminal section of the left lead, and $j = 1$ for the terminal section of the right lead. The unit matrix is omitted in expressions $(H_B^L - E\mathbb{I})$ and $(H_A^R - E\mathbb{I})$; the coefficients in each set, $\left\{ a_{\lambda,+}^{L,\text{pro}} \right\}$, etc., are now listed as columns; Ψ_C is a column vector that stores the wavefunction amplitudes for the central section.

In a case when the width of the central section, N_C , exceeds the width of (at least) one of the leads, i.e., $N_C > N^{(L)}$ or $N_C > N^{(R)}$ (in addition, the leads may be vertically displaced, as in the nanosystem shown in Fig. 8), the blocks occurring near the upper-left or lower-right corner of the main matrix in Eq. (A35) that connect the central section with the leads, namely, \vec{P}_L^\dagger and $\overleftarrow{P}_R^\dagger$ with their hermitian conjugates $\overrightarrow{P}_L^\dagger$, $\overleftarrow{P}_R^\dagger$, are constructed in such a way that the original matrix P'_α is horizontally or vertically expanded and filled with

zeros, namely

$$\overrightarrow{P}_L^\dagger = \begin{pmatrix} 0 & P'_L & 0 \end{pmatrix}, \quad \overleftarrow{P}_R^\dagger = \begin{pmatrix} 0 \\ P'_R \\ 0 \end{pmatrix}, \quad (\text{A36})$$

where the elements in the original block match the existing bonds connecting the lattice sites. (For $N_C = N^{(L)} = N^{(R)}$, we simply have $\overrightarrow{P}_L^\dagger = P'_L$ and $\overleftarrow{P}_R^\dagger = P'_R$.)

In addition, Eq. (A13) with substitutions given by Eq. (A23) for the two leads, guarantees that

$$P_L^\dagger W_{A,-1}^{(L)} + (H_B^L - E)W_{B,-1}^{(L)} = -P'_L W_{A,0}^{(L)}, \quad (\text{A37})$$

$$(H_A^R - E)W_{A,1}^{(R)} + P_R W_{B,1}^{(R)} = -P'_R W_{B,0}^{(R)}, \quad (\text{A38})$$

allowing some further simplification of Eq. (A35).

We now introduce the $(N_{\text{pro}}^{(L)} + N_{\text{pro}}^{(R)}) \times (N_{\text{pro}}^{(L)} + N_{\text{pro}}^{(R)})$

scattering matrix,

$$S = \begin{pmatrix} r & t' \\ t & r' \end{pmatrix}, \quad (\text{A39})$$

defined in such a way that

$$\begin{pmatrix} \left\{ b_{\lambda,-}^{L,\text{pro}} \right\} \\ \left\{ b_{\lambda,+}^{R,\text{pro}} \right\} \end{pmatrix} = S \begin{pmatrix} \left\{ a_{\lambda,+}^{L,\text{pro}} \right\} \\ \left\{ a_{\lambda,-}^{R,\text{pro}} \right\} \end{pmatrix}. \quad (\text{A40})$$

$$\begin{pmatrix} -\overrightarrow{P}'_L U_{A,0}^{(L)} & \overrightarrow{P}'_L \\ \overrightarrow{P}'_L^\dagger U_{B,-1}^{(L)} & \\ & H_C - E \\ & & \overleftarrow{P}'_R U_{A,1}^{(R)} \\ & & \overleftarrow{P}'_R^\dagger & -\overleftarrow{P}'_R^\dagger U_{B,0}^{(R)} \end{pmatrix} \begin{pmatrix} r & t' \\ \left\{ \Psi_C^{(l)} \right\} \\ t & r' \end{pmatrix} = \begin{pmatrix} P'_L V_{A,0}^{(L)} & 0 \\ -\overrightarrow{P}'_L^\dagger V_{B,-1}^{(L)} & 0 \\ 0 & 0 \\ 0 & -\overleftarrow{P}'_R V_{A,1}^{(R)} \\ 0 & P'_R^\dagger V_{B,0}^{(R)} \end{pmatrix}, \quad (\text{A41})$$

where $\left\{ \Psi_C^{(l)} \right\}$ is the set of wavefunctions for the central section, for $l = 1 \dots N_{\text{pro}}^{(L)} + N_{\text{pro}}^{(R)}$, stored as columns. In the above, we used Eqs. (A37), (A38).

The rank of the main matrix in Eq. (A41) is equal to $N_{\text{pro}}^{(L)} + 2N_C M + N_{\text{pro}}^{(R)}$, where M denotes the number of vertical sections, each containing (up to) $2N_C$ lattice sites. Although the shape of the central section is — in principle — irregular, a site-numbering scheme analogous to that used for the leads can be applied. In case of a considerable number of disconnected lattice sites, an additional enumeration for the central part can be applied to eliminate the matrix elements corresponding to disconnected sites and to reduce the rank of the main matrix.

For the total number of sites $2N_C M < 5 \times 10^5$, such as in the numerical examples presented in the main text, one can use standard linear-algebra software to solve the linear system given by Eq. (A41) numerically and find the unknowns, including all elements of the scattering matrix S (A39). We used the double precision LAPACK routine `zgbstv`, see Ref. [84], which employs the band storage scheme for the main matrix with $2N_C - 1$ subdiagonals and $2N_C - 1$ superdiagonals. Assuming that the proportions of the middle section are not very different from those of the square, i.e., $N_C \sim M \sim \sqrt{N_{\text{tot}}}$ (with the total number of sites N_{tot}) we can estimate the computational complexity to be $\mathcal{O}(N_{\text{tot}}^2)$, which is equivalent to the complexity of the more commonly used recursive Green's

function method [85]. Since the normal modes in the left and right leads are calculated independently, we can validate the final numerical output by checking the unitarity condition for the scattering matrix, $SS^\dagger = S^\dagger S = \mathbb{I}$. The deviation from unitarity is quantified by

$$\varepsilon_S = \max \left\{ |(S^\dagger S)_{ll'} - \delta_{ll'}|, 1 \leq l, l' \leq N_{\text{pro}}^{(L)} + N_{\text{pro}}^{(R)} \right\}. \quad (\text{A42})$$

In the numerical problems considered here, the above does not exceed $\varepsilon_S \lesssim 10^{-6}$; the maximal value is approached for the half-disk system, for which the number of propagating modes in the right (i.e., the wider) lead is $52 \leq N_{\text{pro}}^{(R)} \leq 537$ for the energy range of $0.1 \leq (E + V_0)/t_0 \leq 0.9$.

If more than two leads contact the central system, a generalization is straightforward, provided we have a group of (one or more) parallel left leads and a group of parallel right leads. In such a case, the block structure of Eq. (A41) is preserved, and it is only necessary to modify the contents of the blocks connecting the central section and the leads accordingly. For some more complex cases, relevant graph algorithms are implemented in the KWANT package [86].

For much larger systems, the direct lattice approach presented above must be replaced by the method truncating the wavefunction within orthogonal polynomials, such as recently implemented in the KITE software [87].

-
- [1] M. J. Duff, L. B. Okun, and G. Veneziano, Dialogue on the number of fundamental constants, *J. High Energy Phys.* **03**, 023 (2002).
 [2] J.-M. Lévy-Leblond, On the Conceptual Nature of the Physical Constants, in *The Reform of the International System of*

Units (SI): Philosophical, Historical and Sociological Issues (Routledge, London, UK, 2019), pp. 125-149. DOI: <https://doi.org/10.4324/9781351048989>.

- [3] T. Ando, Y. Matsumoto, and Y. Uemura, Theory of Hall Effect in a Two-Dimensional Electron System, *J. Phys. Soc. Jpn.* **39**,

- 279 (1975).
- [4] K. v. Klitzing, G. Dorda, and M. Pepper, New Method for High-Accuracy Determination of the Fine-Structure Constant Based on Quantized Hall Resistance, *Phys. Rev. Lett.* **45**, 494 (1980).
- [5] R. B. Laughlin, Quantized Hall conductivity in two dimensions, *Phys. Rev. B* **23**, 5632(R) (1981).
- [6] D. C. Tsui, H. L. Stormer, and A. C. Gossard, Two-Dimensional Magnetotransport in the Extreme Quantum Limit, *Phys. Rev. Lett.* **48**, 1559 (1982).
- [7] B. D. Josephson, The discovery of tunneling supercurrents, *Rev. Mod. Phys.* **46**, 251 (1974).
- [8] S. Payagala, A. Rigosi, A. Panna, A. Pollarolo, M. Kruskopf, S. Schlamminger, D. Jarrett, R. Brown, R. Elmquist, D. Brown, and D. Newell, Comparison between Graphene and GaAs Quantized Hall Devices with a Dual Probe, *IEEE Trans. Instrum. Meas.* **69**, 9374 (2020).
- [9] Y. Tang, J. Wachter, A. Rufenacht, G. FitzPatrick, and S. Benz, 10 V Programmable Josephson Voltage Standard and its Application in Direct Comparison with the Conventional Josephson Voltage Standard, *IEEE Trans. Instrum. Meas.* **64**, 3458 (2015).
- [10] K. Novoselov, A. Geim, S. Morozov, D. Jiang, M. I. Katsnelson, I. V. Grigorieva, S. V. Dubonos, and A. A. Firsov Two-dimensional gas of massless Dirac fermions in graphene, *Nature* **438**, 197 (2005).
- [11] Y. Zhang, Y.-W. Tan, H. L. Stormer, and P. Kim, Experimental observation of the quantum Hall effect and Berry's phase in graphene, *Nature* **438**, 201 (2005).
- [12] M. Titov and C. W. J. Beenakker, Josephson effect in ballistic graphene, *Phys. Rev. B* **74**, 041401(R) (2006).
- [13] S. Salim, R. Marathe, and S. Gosh, Revisiting Andreev processes in superconductor-graphene-superconductor (SGS) Josephson junctions: comparison with experimental results, *Phys. Scr.* **98**, 065935 (2023).
- [14] M. I. Katsnelson, Zitterbewegung, chirality, and minimal conductivity in graphene, *Eur. Phys. J. B* **51**, 157 (2006).
- [15] M. I. Katsnelson, *The Physics of Graphene*, 2nd ed. (Cambridge University Press, Cambridge, UK, 2020); Chapter 3.
- [16] R. R. Nair, P. Blake, A. N. Grigorenko, K. S. Novoselov, T. J. Booth, T. Stauber, N. M. R. Peres, and A. K. Geim, Fine Structure Constant Defines Visual Transparency of Graphene, *Science* **320**, 1308 (2008).
- [17] H. S. Skulason, P. E. Gaskell, and T. Szkopek, Optical reflection and transmission properties of exfoliated graphite from a graphene monolayer to several hundred graphene layers, *Nanotechnology* **21**, 295709 (2010).
- [18] J. Tworzydło, B. Trauzettel, M. Titov, A. Rycerz, and C. W. J. Beenakker, Sub-Poissonian shot noise in graphene, *Phys. Rev. Lett.* **96**, 246802 (2006).
- [19] R. Danneau, F. Wu, M. F. Craciun, S. Russo, M. Y. Tomi, J. Salmilehto, A. F. Morpurgo, and P. J. Hakonen, Shot Noise in Ballistic Graphene, *Phys. Rev. Lett.* **100**, 196802 (2008).
- [20] A. Rycerz, P. Recher, and M. Wimmer, Conformal mapping and shot noise in graphene, *Phys. Rev. B* **80**, 125417 (2009).
- [21] A. Laitinen, G. S. Paraoanu, M. Oksanen, M. F. Craciun, S. Russo, E. Sonin, and P. Hakonen, Contact doping, Klein tunneling, and asymmetry of shot noise in suspended graphene, *Phys. Rev. B* **93**, 115413 (2016).
- [22] H. Yoshino and K. Murata, Significant Enhancement of Electronic Thermal Conductivity of Two-Dimensional Zero-Gap Systems by Bipolar-Diffusion Effect. *J. Phys. Soc. Jpn.* **84**, 024601 (2015).
- [23] J. Crossno, J. K. Shi, K. Wang, X. Liu, A. Harzheim, A. Lucas, S. Sachdev, P. Kim, T. Taniguchi, K. Watanabe, T. A. Ohki, and K. C. Fong, Observation of the Dirac fluid and the breakdown of the Wiedemann-Franz law in graphene, *Science* **351**, 1058 (2016).
- [24] A. Rycerz, Wiedemann-Franz Law for Massless Dirac Fermions with Implications for Graphene, *Materials* **14**, 2704 (2021).
- [25] Y.-T. Tu and S. Das Sarma, Wiedemann-Franz law in graphene, *Phys. Rev. B* **107**, 085401 (2023).
- [26] G. W. Semenoff, Condensed-Matter Simulation of a Three-Dimensional Anomaly, *Phys. Rev. Lett.* **53**, 2449 (1984).
- [27] D. P. Di Vincenzo, E. J. Mele, Self-consistent effective-mass theory for intralayer screening in graphite intercalation compounds, *Phys. Rev. B* **29**, 1685 (1984).
- [28] A. Rycerz and P. Witkowski, Sub-Sharvin conductance and enhanced shot noise in doped graphene, *Phys. Rev. B* **104**, 165413 (2021).
- [29] A. Rycerz and P. Witkowski, Theory of sub-Sharvin charge transport in graphene disks, *Phys. Rev. B* **106**, 155428 (2022).
- [30] Yu. V. Sharvin, A possible method for studying Fermi surfaces, *Zh. Eksp. Teor. Fiz.* **48**, 984 (1965) [*Sov. Phys. JETP* **21**, 655 (1965)].
- [31] B. J. van Wees, H. van Houten, C. W. J. Beenakker, J. G. Williamson, L. P. Kouwenhoven, D. van der Marel, and C. T. Foxon, Quantized conductance of point contacts in a two-dimensional electron gas, *Phys. Rev. Lett.* **60**, 848 (1988).
- [32] L. I. Glazman, G. B. Lesovik, D. E. Khmel'nitskii, and R. I. Shekhter, Reflectionless quantum transport and fundamental ballistic-resistance steps in microscopic constrictions, *Pisma Zh. Eksp. Teor. Fiz.* **48**, 218 (1988) [*JETP Lett.* **48**, 238 (1988)].
- [33] For the disk geometry, the width W needs to be replaced with the inner lead circumference $2\pi R_i$.
- [34] A. Rycerz, K. Rycerz, and P. Witkowski, Thermoelectric Properties of the Corbino Disk in Graphene, *Materials* **16**, 4250 (2023).
- [35] A. Rycerz, K. Rycerz, and P. Witkowski, Sub-Sharvin Conductance and Incoherent Shot-Noise in Graphene Disks at Magnetic Field, *Materials* **17**, 3067 (2024).
- [36] S. Das Sarma and K. Yang, The enigma of the $\nu=0$ quantum Hall effect in graphene, *Solid State Commun.* **149**, 1502 (2009).
- [37] A. Rycerz, Magnetoconductance of the Corbino disk in graphene, *Phys. Rev. B* **81**, 121404(R) (2010).
- [38] Y. Zeng, J. I. A. Li, S. A. Dietrich, O. M. Ghosh, K. Watanabe, T. Taniguchi, J. Hone, and C. R. Dean, High-Quality Magneto-transport in Graphene Using the Edge-Free Corbino Geometry, *Phys. Rev. Lett.* **122**, 137701 (2019).
- [39] D. Suszalski, G. Rut, and A. Rycerz, Mesoscopic valley filter in graphene Corbino disk containing a p-n junction *J. Phys. Mater.* **3**, 015006 (2020).
- [40] M. Kamada, V. Gall, J. Sarkar, M. Kumar, A. Laitinen, I. Gornyi, and P. Hakonen, Strong magnetoresistance in a graphene Corbino disk at low magnetic fields, *Phys. Rev. B* **104**, 115432 (2021).
- [41] C. Kittel, *Introduction to Solid State Physics*, 8th ed. (John Wiley and Sons: New York, NY, USA, 2005); Chapter 6.
- [42] C. T. White and T. N. Todorov, Carbon nanotubes as long ballistic conductors, *Nature* **393**, 240 (1998).
- [43] N. Agraït, A. Levy Yeyati, J. M. van Ruitenbeek, Quantum properties of atomic-sized conductors, *Phys. Rep.* **377**, 81 (2003).
- [44] R. Landauer, Spatial Variation of Currents and Fields Due to Localized Scatterers in Metallic Conduction, *IBM J. Res. Dev.* **1**, 223 (1957).
- [45] M. Büttiker, Y. Imry, R. Landauer, and S. Pinhas, Generalized many-channel conductance formula with application to small rings, *Phys. Rev. B* **31**, 6207 (1985).

- [46] C. Kumar, J. Birkbeck, J. A. Sulpizio, D. J. Perello, T. Taniguchi, K. Watanabe, O. Reuven, T. Scaffidi, A. Stern, A. K. Geim, and S. Ilani, Imaging hydrodynamic electrons flowing without Landauer-Sharvin resistance, *Nature* **609**, 276 (2022).
- [47] Y. Cao, V. Fatemi, A. Demir, S. Fang, S. L. Tomarken, J. Y. Luo, J. D. Sanchez-Yamagishi, K. Watanabe, T. Taniguchi, E. Kaxiras, R. C. Ashoori, and P. Jarillo-Herrero, Correlated insulator behaviour at half-filling in magic-angle graphene superlattices, *Nature* **556**, 80 (2018).
- [48] Y. Cao, V. Fatemi, S. Fang, K. Watanabe, T. Taniguchi, E. Kaxiras, and P. Jarillo-Herrero, Unconventional superconductivity in magic-angle graphene superlattices, *Nature* **556**, 43 (2018).
- [49] M. Fidrysiak, M. Zegrodnik, and J. Spalek, Unconventional topological superconductivity and phase diagram for an effective two-orbital model as applied to twisted bilayer graphene, *Phys. Rev. B* **98**, 085436 (2018).
- [50] Y. V. Nazarov and Y. M. Blanter, *Quantum Transport: Introduction to Nanoscience* (Cambridge University Press, Cambridge, UK, 2009); Chapter 1.
- [51] Strictly speaking, these solutions take the form of linear combinations of two plane waves (with positive and negative k_y), producing standing waves in the y direction, but this detail is irrelevant to the calculations presented below.
- [52] E. C. Kemble, A Contribution to the Theory of the B. W. K. Method, *Phys. Rev.* **48**, 549 (1935).
- [53] N. Takimoto, S. Yamamura, and K. Funayama, Generation of Non-Equilibrium $1/f$ Temperature Noise, *J. Phys. Soc. Jpn.* **62**, 3077 (1993).
- [54] K. Schönhammer, Full counting statistics for noninteracting fermions: Exact results and the Levitov-Lesovik formula, *Phys. Rev. B* **75**, 205329 (2007).
- [55] It should be noted that Eq. (20) is used for the K -valley neighborhood in the dispersion relation; for the K' -valley the matrix σ_y should be replaced by $\sigma_y^* = -\sigma_y$.
- [56] M. V. Berry and R. J. Mondragon, Neutrino billiards: time-reversal symmetry-breaking without magnetic fields, *Proc. R. Soc. Lond. A* **412**, 53 (1987).
- [57] T. R. Robinson, On Klein tunneling in graphene, *Am. J. Phys.* **80**, 141 (2012).
- [58] C. Gutiérrez, L. Brown, C. J. Kim, J. Park, and A. N. Pasupathy, Klein tunnelling and electron trapping in nanometre-scale graphene quantum dots, *Nat. Phys.* **12**, 1069 (2016).
- [59] Similar to the Schrödinger equation case, the wave function matching conditions are a consequence of charge conservation. To obtain the current density operator, in the Hamiltonian operator on the left side of Eq. (20), $H = v_F \mathbf{p} \cdot \boldsymbol{\sigma} + V(x)$, we substitute $\mathbf{p} \rightarrow \mathbf{p} + e\mathbf{A}$, and then differentiate the resulting operator $H(\mathbf{A})$ with respect to the vector potential \mathbf{A} . In effect, we obtain $\mathbf{j} = ev_F \boldsymbol{\sigma}$, and therefore the continuity of the current corresponds to the continuity of the components of the wave function (operator \mathbf{j} does not involve differentiation over coordinates).
- [60] S. Datta, *Electronic Transport in Mesoscopic Systems* (Cambridge University Press, Cambridge, UK 1997); Chapter 3.
- [61] A. Schuessler, P. M. Ostrovsky, I. V. Gornyi, and A. D. Mirlin, Full counting statistics in disordered graphene at Dirac point: From ballistics to diffusion, *Phys. Rev. B* **82**, 085419 (2010).
- [62] I. S. Gradshteyn and I. M. Ryzhik, *Table of Integrals, Series, and Products*, Seventh Edition (Academic Press, New York, 2007); Eq. 2.553.3.
- [63] F. Miao, S. Wijeratne, Y. Zhang, U. C. Coskun, W. Bao, C. N. Lau, Phase Coherent Transport in Graphene Quantum Billiards, *Science* **317**, 1530 (2007).
- [64] M. Abramowitz and I. A. Stegun, eds., *Handbook of Mathematical Functions* (Dover Publications, Inc., New York, 1965); Chapter 15.
- [65] L. DiCarlo, J. R. Williams, Y. Zhang, D. T. McClure, C. M. Marcus, Shot Noise in Graphene, *Phys. Rev. Lett.* **100**, 156801 (2008).
- [66] M. I. Katsnelson and F. Guinea, Transport through evanescent waves in ballistic graphene quantum dots, *Phys. Rev. B* **78**, 075417 (2008).
- [67] A. Rycerz and D. Suszalski, Graphene disk in a solenoid magnetic potential: Aharonov-Bohm effect without a two-slit-like setup, *Phys. Rev. B* **101**, 245429 (2020).
- [68] C. W. J. Beenakker and M. Büttiker, Suppression of shot noise in metallic diffusive conductors, *Phys. Rev. B* **46**, 1889(R) (1992).
- [69] K. E. Nagaev, On the shot noise in dirty metal contacts, *Phys. Lett. A* **169**, 103 (1992).
- [70] C. W. J. Beenakker, Random-matrix theory of quantum transport, *Rev. Mod. Phys.* **69**, 731 (1997).
- [71] A. Rycerz, J. Tworzydło, and C. W. J. Beenakker, Valley filter and valley valve in graphene, *Nat. Phys.* **3**, 172 (2007).
- [72] M. Wimmer, Í. Adagideli, S. Berber, D. Tománek, and K. Richter, Spin Currents in Rough Graphene Nanoribbons: Universal Fluctuations and Spin Injection, *Phys. Rev. Lett.* **100**, 177207 (2008).
- [73] M. M. Grujić, M. Ž. Tadić, and F. M. Peeters, Spin-Valley Filtering in Strained Graphene Structures with Artificially Induced Carrier Mass and Spin-Orbit Coupling, *Phys. Rev. Lett.* **113**, 046601 (2014).
- [74] W. Bao, G. Liu, Z. Zhao, H. Zhang, D. Yan, A. Deshpande, B. J. LeRoy, and C. N. Lau, Lithography-free Fabrication of High Quality Substrate-supported and Freestanding Graphene devices, *Nano Res.* **3**, 98 (2010).
- [75] G. Giovannetti, P. A. Khomyakov, G. Brocks, V. M. Karpan, J. van den Brink, and P. J. Kelly, Doping Graphene with Metal Contacts, *Phys. Rev. Lett.* **101**, 026803 (2008).
- [76] T. Cusati, G. Fiori, A. Gahoi, V. Passi, M. C. Lemme, A. Fortunelli, and G. Iannaccone, Electrical properties of graphene-metal contacts, *Sci. Rep.* **7**, 5109 (2017).
- [77] T. Ando, Quantum point contacts in magnetic fields, *Phys. Rev. B* **44**, 8017 (1991).
- [78] It can be further approximated as $N_{\text{approx}} = 2KW_{\text{infty}}/\pi$ with $K = |E + V_{\infty}|/\hbar v_F$, giving $N_{\text{approx}} \simeq 130$ for $E = 0$ and $V_{\infty} = t_0/2$; the actual number of propagating modes $N_{\text{open}}^{(\infty)} \geq N_{\text{approx}}$ (if $|E + V_{\infty}| \lesssim t_0$) due to the trigonal warping.
- [79] K. Wakabayashi and T. Aoki, Electrical conductance of zigzag nanographite ribbons with locally applied gate voltage, *Int. J. Mod. Phys. B* **16**, 4897 (2002).
- [80] K. Wakabayashi, K. Sasaki, T. Nakanishi, and T. Enoki, Electronic states of graphene nanoribbons and analytical solutions, *Sci. Technol. Adv. Mater.* **11** 054504 (2010).
- [81] M. Ezawa, Monolayer Topological Insulators: Silicene, Germanene, and Stanene, *J. Phys. Soc. Jpn.* **84**, 121003 (2015).
- [82] T. Hartman and Z. Sofer, Beyond Graphene: Chemistry of Group 14 Graphene Analogues: Silicene, Germanene, and Stanene, *ACS Nano* **13**, 8566 (2019).
- [83] S. Kashiwaya, Y. Shi, J. Lu, D. G. Sangiovanni, G. Greczynski, M. Magnuson, M. Andersson, J. Rosen, and L. Hultman, Synthesis of goldene comprising single-atom layer gold, *Nat. Synth.* **3**, 744 (2024).
- [84] E. Anderson, Z. Bai, C. Bischof, S. Blackford, J. Demmel, J. Dongarra, J. D. Croz, A. Greenbaum, S. Hammarling, A. McKenney, et al., *LAPACK Users' Guide*, Third Edition (Society for Industrial and Applied Mathematics, Philadelphia, PA,

- USA, 1999).
- [85] C. H. Lewenkopf, E. R. Mucciolo, The recursive Green's function method for graphene, *J. Comput. Eletron.* **12**, 203 (2013).
- [86] C. W. Groth, M. Wimmer, A. R. Akhmerov, and X. Waintal, Kwant: a software package for quantum transport, *New J. Phys.* **16**, 063065 (2014).
- [87] S. M. João, M. Anđelković, L. Covaci, T. G. Rappoport, J. M. V. P. Lopes, and A. Ferreira, KITE: high-performance accurate modelling of electronic structure and response functions of large molecules, disordered crystals and heterostructures, *R. Soc. Open Sci.* **7**, 191809 (2020).